



1 **Dating circulations of hydrothermal fluids in the crystalline
2 basements of unconformity-related metallic deposits using in
3 situ Rb/Sr geochronology : proof of concept**

4

5 Quentin Boulogne^{1,2*}, Gaétan Milesi^{1,2}, Chantal Peiffert¹, Emmy Fischer^{1,2}, Christophe
6 Ballouard¹, Mehdi Serdoun^{1,3}, Thomas Obin^{1,2}, Andréï Lecomte¹, Pierre Martz³, Andrew
7 Kaczowka⁴ and Julien Mercadier^{1,2}

8 ¹*Université de Lorraine, CNRS, GeoRessources, F-54000 Nancy, France*

9 ²*LabCom CREGU, GeoRessources, CNRS, Université de Lorraine, Vandœuvre-lès-Nancy, France*

10 ³*Orano Canada, Saskatoon, Canada*

11 ⁴*Cameco Corporation, Saskatoon, Canada*

12 *Correspondence to:* Quentin Boulogne (quentin.boulogne@univ-lorraine.fr)

13

14 **Abstract.** The use of *in situ* Rb-Sr geochronology has boomed in recent years following its implementation using
15 LA-ICP-QQQ-MS technology, which enables fast, *in situ* analyses at the micron scale on selected minerals. The
16 Rb-Sr geochronometer applied to micas is now commonly used to date the crystallization or cooling of
17 metamorphic and magmatic rocks, based on the assumptions of a closed isotopic system after passing the closure
18 temperature and of a homogeneous Sr isotopic composition at the time of crystallization. *In situ* Rb-Sr
19 geochronology applied to micas and related alteration products in geological contexts involving hydrothermal fluid
20 circulation affecting micas after crystallization could provide a new way to decipher the timing and duration of
21 fluid circulation in various settings such as mountain belts or sedimentary basins. The behavior and applicability
22 of the Rb-Sr system in such contexts are, however, poorly understood, as the system may be partially reopened
23 with differential redistribution of Rb and Sr at the grain scale. To test this hypothesis, we selected a case study
24 related to unconformity-related U deposits from the Athabasca Basin (Canada), which formed through intense
25 hydrothermal fluid circulation at the interface between crystalline basement and siliciclastic sedimentary rocks and
26 represent archetypes of unconformity-related metallic deposits. Muscovite grains from metamorphic and magmatic
27 rocks were targeted across a range of alteration states, from hydrothermally unaltered to strongly altered domains.
28 We focused on a specific hydrothermal alteration linked to the formation of hydrothermal illite and sudoite at the
29 expense of metamorphic or magmatic minerals. In unaltered zones, muscovite displayed variable but high Rb/Sr
30 ratios, whereas the $^{87}\text{Sr}/^{86}\text{Sr}$ intercepts derived from Rb-Sr regressions were scattered and were not interpreted as
31 meaningful initial isotopic compositions. The resulting ages ranged from ca. 1870 to ca. 1720 Ma and were
32 consistent with the geological context. In distal-to-proximal alteration halos of U deposits, muscovite and related
33 alteration products yielded lower $^{87}\text{Rb}/^{86}\text{Sr}$ ratios and highly variable regression intercepts. The mean age
34 calculated across the different samples and investigated sites clustered around ~1640 Ma, a value previously



35 obtained by Ar-Ar geochronology on illite and U-Pb geochronology on other hydrothermal phases and proposed
36 to correspond to a major hydrothermal event linked to a geodynamic reorganization affecting the Canadian Shield
37 at the circum-Laurentian scale. The ~1640 Ma age is geologically meaningful in the studied context and is
38 interpreted as reflecting partial, micrometric-scale resetting of the Rb-Sr system in muscovite during this
39 hydrothermal event. The wide range of regression intercept values commonly observed in disturbed Rb-Sr systems
40 is interpreted as an apparent result of open-system behavior, reflecting partial system reopening and non-
41 conservative redistribution of Rb and Sr at the grain scale, rather than as a physically meaningful initial isotopic
42 composition. These results demonstrate that detailed analysis of Rb-Sr system perturbations in altered muscovite
43 and related alteration products can constrain the timing of ancient hydrothermal activity and the spatial dynamics
44 of fluid-rock interaction. This approach provides a valuable complement to conventional fluid-tracing methods
45 and opens new perspectives for reconstructing paleo-hydrothermal systems in ancient basement terrains.

46 Key words: Rb-Sr geochronology, Muscovite alteration, Hydrothermal fluid circulation, Athabasca Basin, *In situ*
47 LA-ICP-MS, Isotopic resetting

48 1. Introduction

49 Crystalline basements are environments in which multiple types of fluids can circulate over geological timescales,
50 depending on the conditions under which these basements formed and later evolved. These fluids may originate
51 from highly diverse sources (magmatic, metamorphic, basin-derived, meteoric, etc.) and display a wide range of
52 physicochemical properties and compositions. Their circulation is primarily driven by first-order geological
53 processes (geodynamic, tectonic, sedimentological, etc.) and is considered to be largely controlled by structural
54 networks, particularly faults, that enhance permeability and enable surface-derived fluids, for instance, to reach
55 depths of several kilometers. Beyond faults and their associated damage zones, fluids may also migrate through
56 broader networks of inherited microfractures and permeable structures within crystalline rocks (e.g., Sibson, 1990;
57 Faulkner et al., 2010; Viswanathan et al., 2022). These fluids can remain stored for millions of years and may be
58 mobilized and/or mixed in response to changes in mechanical conditions (e.g., Anders et al., 2014; Frey et al.,
59 2022). They interact in various ways with the lithologies and mineral assemblages of the basement, inducing
60 mineralogical, chemical, and/or isotopic modifications that may ultimately lead to the formation of various
61 resources such as metallic deposits or reservoirs of geothermal waters and metal-rich brines (e.g., Etheridge et al.,
62 1983; Yardley, 1983). Over the past decades, scientific studies have demonstrated, contrary to earlier assumptions,
63 that crystalline basements represent favorable environments for fluid circulation and storage (e.g., Juhász et al.,
64 2002; Walter et al., 2018).

65 Fluids therefore play a key role in the evolution of crystalline basements, and it is of major scientific importance
66 to identify and date the various episodes of fluid circulation in these environments (e.g., Sibson, 1990; Holness,
67 2000; Yardley and Bodnar, 2014). Radiometric dating represents a first-order challenge in such contexts, where
68 multiple fluid types may have circulated successively through the same zone in response to large-scale (tectonic)
69 or local-scale (fault-related) geological changes (e.g., Rasmussen et al., 2023; Saito et al., 2018; Weinberg et al.,
70 2020). Each fluid-flow event can leave specific mineralogical markers, often small in size and intermixed with
71 pre-existing minerals. Isotopic dating is also challenging due to the presence of inherited minerals and initial
72 isotopic signatures within the basement, which must be distinguished from those specifically related to each fluid
73 episode (e.g., Dodson, 1973; Grand'Homme et al., 2016). Significant advances have been achieved through the



74 development and application of *in situ* U-Pb dating of hydrothermal minerals (phosphates, titanium oxides,
75 carbonates, etc.) (e.g., Rasmussen et al., 2001; Rasmussen et al., 2006; Davis et al., 2011; Rabiei et al., 2017;
76 Adlakha and Hattori, 2021). Recent methodological developments in K-Ar dating of clay minerals emphasize the
77 systematic separation of multiple grain-size fractions, combined with detailed mineralogical, crystallographic, and
78 polytype characterization (1Md-1M vs. 2M1 illite), in order to deconvolve mixed detrital and authigenic illite
79 populations and extract meaningful age information related to distinct crystallization or recrystallization events
80 (e.g., Reynolds and Thomson, 1993; Velde and Christophe, 1996; Clauer et al., 1997; Hueck et al., 2022; Gerardin
81 et al., 2024). Such an integrated K-Ar-polytype approach has notably been applied to fault gouges, where dating
82 different clay fractions allows the timing of synkinematic hydrothermal fluid-faulting episodes to be constrained,
83 thereby resolving the temporal evolution of brittle deformation and fluid circulation in fault-controlled
84 hydrothermal systems (e.g., Aldega et al., 2019; Campanha et al., 2026; Schmitz et al., 2025). A limitation of this
85 approach lies in the fact that these minerals are accessory phases, generally present in limited quantities and/or at
86 small spatial scales, which creates difficulties in targeting and identification and often requires the use of costly
87 and time-intensive microscopic techniques, or that they are restricted to specific lithologies or structural contexts.
88 The development of *in situ* Rb-Sr geochronology over the past decade has led to a resurgence of interest in the use
89 of micas and feldspars as chronometers in crystalline basements, where they are ubiquitous (e.g., Gyomlai et al.,
90 2023; Jegal et al., 2022; Mlynarska et al., 2024; Muñoz-Montecinos et al., 2024). Several studies have
91 demonstrated the relevance of this approach for dating magmatic (e.g., Larsen and Sundvoll, 2008; Tichomirowa
92 et al., 2019; Scott Anderson et al., 2015; Bevan et al., 2021) or metamorphic (e.g., Jenkin et al., 2001; Willigers et
93 al., 2004; Eberlei et al., 2015) events responsible for the crystallization of these minerals, as well as for dating
94 subsequent thermal and/or fluid-related events that affected these primary minerals after their formation, such as
95 in the context of hydrothermal gold deposits (Olierook et al., 2020; Liebmann et al., 2022; Ribeiro et al., 2023a,
96 b; Qiu et al., 2024). These pioneering studies have suggested that the Rb-Sr chronometer may be partially to
97 completely reset within inherited minerals during post-crystallization fluid and/or thermal events. Furthermore,
98 this approach could allow direct dating of hydrothermal circulations affecting basement environments using
99 metamorphic and/or magmatic minerals and their alteration products.
100 The objective of this contribution is to test this hypothesis in the context of paleo-hydrothermal systems developed
101 at the interface between a crystalline basement and a sedimentary basin. These systems have generated, throughout
102 Earth history, metallic deposits of various commodities such as Pb, Zn, Cu, U, F, and Ba (e.g., Boiron et al., 2010;
103 Cathelineau et al., 2012; Oummouch et al., 2017). The case study focuses on the unconformity-related uranium
104 deposits of the Athabasca Basin (Saskatchewan, Canada), which host the world's highest-grade uranium deposits.
105 These deposits have been the subject of intensive scientific research for over sixty years, and much is known about
106 the typology, age, and geological context of the associated alterations and mineralization. Uranium mineralization
107 formed during hydrothermal episodes that postdated basin deposition and were active in both basin and basement
108 settings. These events led to the formation of localized zones of clay-rich alteration, mainly illite and chlorite,
109 surrounding the orebodies, and are thought to result from interactions between host rocks and evaporitic brines
110 derived from the basin. Although the formation mechanisms are broadly similar to those responsible for other
111 unconformity-related metalliferous deposits worldwide, the interpretation of geochronological data in such long-
112 lived and overprinted hydrothermal systems remains problematic. Existing chronometers commonly yield complex
113 or equivocal age signatures that do not directly correspond to discrete alteration events. This persistent challenge



114 underscores the need to evaluate alternative mineral-isotope systems, such as Rb-Sr signatures recorded by
115 basement micas and related hydrothermal products, to more accurately constrain the chronology of alteration
116 associated with the uranium mineralization.

117 **2. Geological settings**

118 **2.1. Geological history of the Wollaston-Mudjatik Transition Zone**

119 The Athabasca Basin unconformably overlies the Archean to Paleoproterozoic basement rocks known as the
120 Western Churchill Structural Province (WSP). The WSP is divided into two lithostructural subprovinces: the Rae
121 Subprovince to the west and the Hearne Subprovince to the east (Annesley et al., 2005) (Fig. 1A). The Trans-
122 Hudson Orogeny (THO), which represents a major Paleoproterozoic belt, is linked to the collision between the
123 Rae, Hearne, and Superior cratons. The beginning of this orogeny is characterized by the amalgamation between
124 1920 and 1840 Ma of the Rae and Hearne cratons, leading to the formation of the Western Churchill Structural
125 Province (WSP) and to an oceanic arc in the Manikewan Ocean (Ansdel, 2005; Corrigan, 2012; Corrigan et al.,
126 2005, 2009). The gradual closure of the Manikewan Ocean led to the successive accretion of juvenile crustal
127 segments between 1880 and 1860 Ma. The final stage of the THO resulted in the complete closure of the
128 Manikewan Ocean and in the continental collision between the margin of the Hearne craton bordered by the
129 accreted juvenile arcs and the northern edge of the Superior craton between 1830 and 1800 Ma (Corrigan et al.,
130 2009). Finally, the latter stages of THO deformation are marked by the emplacement at ca. 1800 and 1720 Ma of
131 pegmatites and aplites, in relation to sinistral deformation along shear bands in a transpressional context (e.g.,
132 Chiarenzelli, 1989; Bickford et al., 1990; Chiarenzelli et al., 1998; Bickford et al., 2005; Schneider et al., 2007).

133 The western margin of the Hearne Craton comprises two distinct domains of Paleoproterozoic age: the Mudjatik
134 domain and the Wollaston domain (Fig. 1A). The Mudjatik domain is predominantly composed of Archean
135 tonalite-trondhjemite felsic gneiss domes (2.64-2.58 Ga; Annesley et al., 1997a, 1997b, 1999). In contrast, the
136 Wollaston domain is composed mainly of Paleoproterozoic metasediments attributed to the Wollaston Supergroup
137 (deposited at ca. 2050-1860 Ma; Yeo and Delaney, 2007; Tran et al., 2008), including paragneisses, banded iron
138 formations, quartzites, and marbles. These units are interpreted as evidence of sedimentation initially controlled
139 by a passive-margin setting, which evolved into a back-arc basin and then into a foreland basin in response to
140 tectonic processes related to the collision phase (Annesley et al., 2005; Jeanneret et al., 2016). The two lithotectonic
141 domains are separated by the Wollaston-Mudjatik Transition Zone (WMTZ), within which the present study area
142 is located (Fig. 1A). This zone exhibits an anastomosed structure oriented from northeastern to southwestern, a
143 trait that was inherited from the THO. The deformation phases associated with the various stages of THO formation
144 mentioned above can be observed within this zone.

145 The basement rocks underwent three tectono-metamorphic events. The first event (M1-D1) is dated from ca. 1840
146 to 1813 Ma based on U-Pb dating of monazite and zircon from migmatitic metapelites of the Wollaston
147 Supergroup. These rocks host a garnet-cordierite ± sillimanite assemblage that experienced partial melting at peak
148 conditions of 750-825 °C and \leq 10 kbar (Annesley et al., 1992, 1997a,b,c, 1999a,b; Jeanneret et al., 2017; Toma et
149 al., 2024). The second event (M2-D2), dated from ca. 1813 to 1770 Ma, is recorded within migmatites and
150 pegmatites. It corresponds to an isothermal decompression down to 5-9 kbar at temperatures of 750-825 °C, within
151 the stability field of cordierite under suprasolidus conditions, as constrained by U-Pb dating of monazite and zircon



152 (Annesley et al., 1992, 1997a,b,c, 1999a,b; Jeanneret et al., 2017; Toma et al., 2024). The third event corresponds
153 to an exhumation and orogenic cooling phase. Although its onset is poorly constrained, this phase is generally
154 considered to extend from ca. 1.77 Ga (750 °C, 5 kbar) to ca. 1.72 Ga (350 °C, 2 kbar), as documented by several
155 studies (Annesley and Madore, 1994; Annesley et al., 1992, 1997a,b,c, 2005; Jeanneret et al., 2017; Martz et al.,
156 2017). This exhumation phase is characterized by pronounced retrograde transformations linked to early-stage
157 hydrothermal activity. These include the breakdown of cordierite in favour of phyllosilicates, biotite chloritization,
158 remobilization and precipitation of sulfides, graphite, and muscovite, circulation of quartz-rich fluids, and
159 dissolution-reprecipitation processes affecting monazite and zircon (Card, 2012, 2013; Card and Noll, 2016). This
160 phase is further constrained by cooling ages derived from biotite Rb-Sr (Worden et al., 1985; Schneider et al.,
161 2007), muscovite K-Ar (Philippe et al., 1993), and muscovite Ar-Ar systems (Alexandre et al., 2009).

162 **2.2. Geological history of the Athabasca Basin**

163 The Paleoproterozoic to Mesoproterozoic Athabasca Basin is a large intracratonic basin located in northern
164 Saskatchewan and Alberta (Ramaekers et al., 2007). The sedimentary sequence of this basin, known as the
165 Athabasca Supergroup, was deposited between ca. 1760-1720 Ma (Ramaekers et al., 2007; Jeanneret et al., 2016)
166 and 1541 Ma for the youngest known age (Creaser and Stasiuk, 2007). Stratigraphic, geochronological, and fluid-
167 inclusion P-T data indicate that the basin reached a maximum depth of 2 to 5 km depending on the methods
168 considered (Pagel et al., 1975; Chi et al., 2018), with a preserved thickness of 1.5 km today (Hobson and MacAuley,
169 1969). The stratigraphic sequence is organized into four major clastic sedimentary sequences that record a
170 progressive deepening of the basin (Jefferson et al., 2007b). The first sequence, represented by the Fair Point
171 Formation, consists of conglomerates and quartz-pebble arenites infilling the Jackfish Sub-basin, located in the
172 western part of the basin, during the initial sag phase around 1760 Ma (e.g., Ramaekers et al., 2007; Pehrsson et
173 al., 2023). The second sequence, including the Smart/Read and Manitou Falls formations, fills the Cree Sub-basin,
174 situated in the eastern and southeastern parts of the basin, and reflects the development of a shallow half-graben
175 with NW-directed palaeoflow between 1680 and 1650 Ma (Ramaekers et al., 2007; Jeanneret et al., 2016; Pehrsson
176 et al., 2023). The third sequence, represented by the Lazenby Lake and Wolverine Point formations, shows vertical
177 fining and records a major paleoenvironmental shift around 1640 Ma, characterized by abrupt deepening in the
178 western basin, a marine incursion, and a transition to axial palaeocurrents sourced from the north or east (Rainbird
179 et al., 2007; Ramaekers et al., 2007), as indicated by vitric tuff layers dated at 1644 ± 13 Ma (U-Pb zircon; Rainbird
180 et al., 2007). The final sequence, which includes the Locker Lake, Otherside, Douglas, and Carswell formations,
181 reflects detrital and marine sedimentation during continued subsidence and tectonic reorganization associated with
182 the Kuungmi rifting (Pehrsson et al., 2023), notably recorded by organic-rich black shales of the Douglas
183 Formation dated by Re-Os at 1541 ± 13 Ma (Creaser and Stasiuk, 2007). Overall, the basin maintains a largely
184 coherent oval geometry with minimal deformation, except for the Ordovician Carswell impact structure, which
185 locally disrupts the Athabasca Supergroup (Ramaekers et al., 2007; Pehrsson et al., 2023).

186 **2.3. Petrographic and metallogenic characteristics of unconformity-related uranium deposits in the**
187 **Athabasca Basin**

188 The Athabasca Basin unconformity-related uranium deposits are globally renowned for their exceptionally high
189 grades, reaching up to 20 wt. % U_3O_8 . The principal uranium deposits are concentrated in the eastern part of the
190 Athabasca Basin and are spatially associated with a NE-SW-trending anastomosed transition zone inherited from



191 the Trans-Hudsonian Orogeny (THO), commonly referred to as the Wollaston-Mudjatik Transition Zone. This
192 structural corridor comprises a ca. 50-km-wide network of graphite-rich shear zones, typically described as
193 graphite conductors, as they exhibit high electrical conductivity, a physical property that allows their detection by
194 electromagnetic geophysical methods used for uranium exploration (Fig. 1). The uranium deposits are spatially
195 associated with graphite-rich shear zones, and uranium orebodies show diverse morphologies and structural
196 associations depending on their location: (i) at the unconformity, within the first meters of sandstones and
197 conglomerates; (ii) within the basement, extending several hundred meters below the unconformity along shear
198 zones; or (iii) as perched deposits located tens to hundreds of meters above the unconformity within the
199 sedimentary sequence. The mineralized zones are surrounded by hydrothermal alteration halos that can extend
200 several tens of meters into both the basin and the basement and serve as critical geochemical and mineralogical
201 guides for U exploration. In the basin, alteration halos overlying basement-hosted deposits or surrounding
202 sandstone-hosted mineralization are dominated by illite, with variable amounts of kaolinite, sudoite (tri-
203 dioctahedral Mg-chlorite), and dravite (magnesian tourmaline), depending on the deposit.

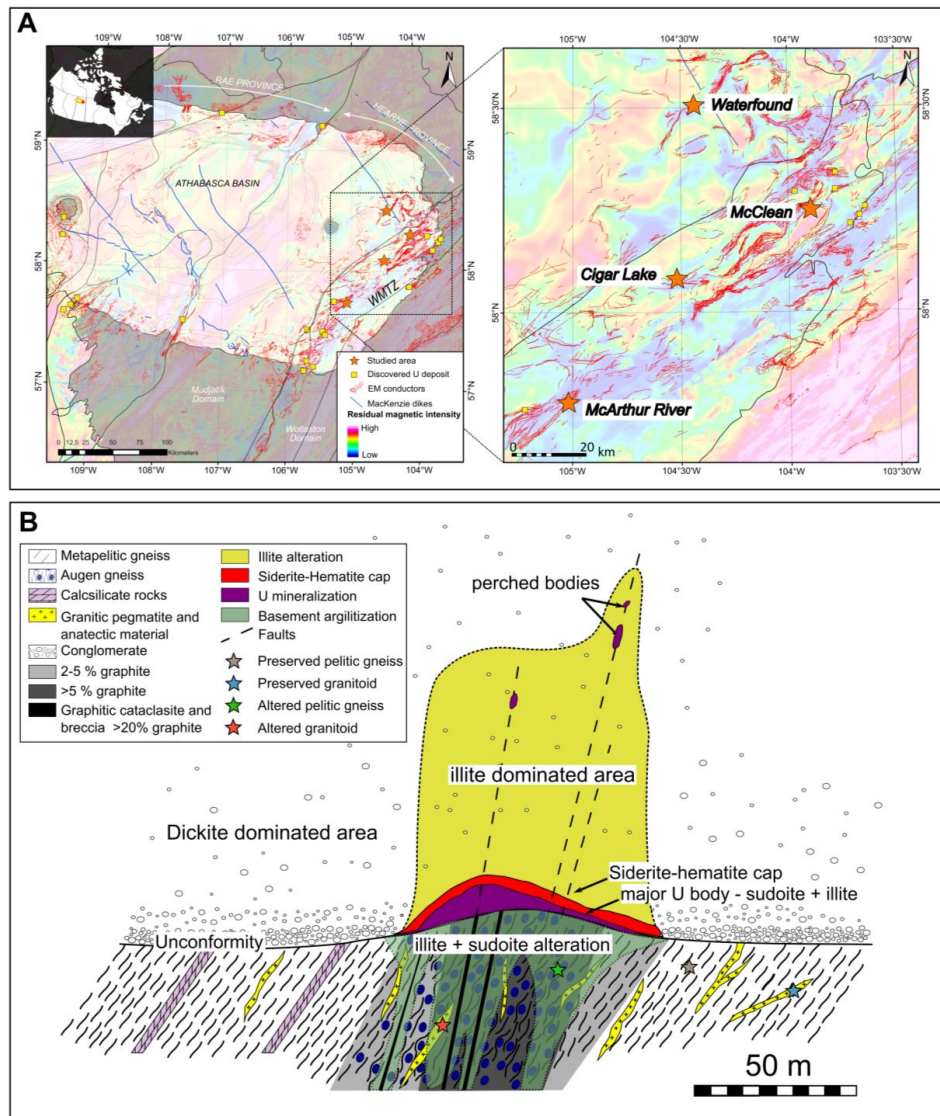
204 Within the basement, three principal alteration types are superimposed, as exemplified by the world-class Cigar
205 Lake deposit (Fig. 1C). The first type corresponds to retrograde metasomatic alteration related to the final
206 exhumation and orogenic cooling phase of the Trans-Hudsonian Orogeny (THO). It is marked by partial to
207 complete biotite chloritization, discrete quartz and muscovite crystallization, and hydrothermal graphite formation.
208 These alteration types and their associated petrographic features have been extensively documented in the vicinity
209 of unconformity-related uranium deposits within the Athabasca Basin (e.g., Carl et al., 1992; Derome et al., 2005;
210 Cloutier et al., 2011; Mercadier et al., 2011; Alexandre et al., 2012; Adlakha et al., 2015; Martz et al., 2019a;
211 Menier et al., 2020; Powell et al., 2022). The second type corresponds to regolithic alteration developed within the
212 upper tens of meters of the basement following its exhumation after the Trans-Hudsonian Orogeny. It is
213 characterized by a laterally correlative weathering profile comprising four zones: (i) a bleached kaolinite-rich and
214 hematite-depleted zone at the unconformity; (ii) a highly oxidized hematite-rich zone; (iii) a red-green transitional
215 zone characterized by hematite and chlorite; and (iv) a thicker green-to-red zone enriched in illite, chlorite, and
216 hematite (e.g., Macdonald, 1980; Halter, 1988). The third type corresponds to post-basin-deposition hydrothermal
217 alteration, which represents the most extensive alteration type. It is proposed to be linked with uranium
218 mineralization and is characterized by the massive replacement of primary minerals by an illite- and sudoite-
219 dominated clay assemblage.

220 The main accepted model for the formation of these deposits is known as “diagenetic-hydrothermal” and involves
221 the circulation of oxidized brines of marine origin containing $\text{NaCl}-\text{CaCl}_2$ at temperatures of around 120 to 200°C
222 in the basin and underlying bedrock (Derome et al., 2005; Richard et al., 2011, 2013, 2015). The interaction of
223 these brines with basin and/or basement rocks favors the formation of alteration halos and mobilizes uranium in
224 its oxidized form (U^{6+}), which is transported through fractures and reactivated graphitic structures. Uranium
225 precipitates within structural and physicochemical traps, where dissolved hexavalent uranium (U^{6+}) is reduced to
226 tetravalent uranium (U^{4+}) (Hoeve and Sibbald, 1978; Jefferson et al., 2007).

227 Published absolute ages for the precipitation of primary uranium mineralization at the scale of the basin span a
228 broad range, from ca. 1590 to 1200 Ma. These estimates derive from U-Pb analyses of UO_2 and from K-Ar or Ar-
229 Ar geochronology of clay minerals (Cumming and Krstic, 1992; Philippe et al., 1993; McGill et al., 1993; Fayek



230 et al., 2002b; Alexandre et al., 2009; Cloutier et al., 2011; Powell et al., 2022). Building on these age constraints,
231 an alternative hypothesis invoking an earlier episode of uranium mineralization and/or hydrothermal alteration
232 merits consideration. Numerous studies have shown that U-Pb systematics of uraninite and associated alteration
233 minerals in unconformity-related deposits are commonly overprinted by multiple fluid-flow events, resulting in
234 partial Pb loss and a broad dispersion of apparent ages (Kotzer and Kyser, 1990; Fayek and Kyser, 1997; Fayek et
235 al., 2002a,b; Kyser et al., 2015). Consequently, the existence of an older hydrothermal system, potentially active
236 in the ca. 1640-1680 Ma interval, cannot be ruled out and may be cryptic due to subsequent alteration, uranium
237 remobilization, and isotopic resetting during younger tectono-hydrothermal episodes. This interpretation is
238 consistent with evidence for repeated basin-scale fluid circulation and late-stage meteoric fluid ingress documented
239 in the Athabasca Basin, processes that are known to modify both clay mineral K-Ar/Ar-Ar ages and uraninite U-
240 Pb signatures. A similarly complex temporal evolution is recognized in unconformity-related uranium systems of
241 northern Australia, where *in situ* U-Pb analyses of uraninite suggest initial mineralization or hydrothermal
242 alteration as early as ca. 1680-1640 Ma, followed by multiple younger resetting events extending into the
243 Mesoproterozoic and Paleozoic (Clauer et al., 2015; Skirrow et al., 2016).



244

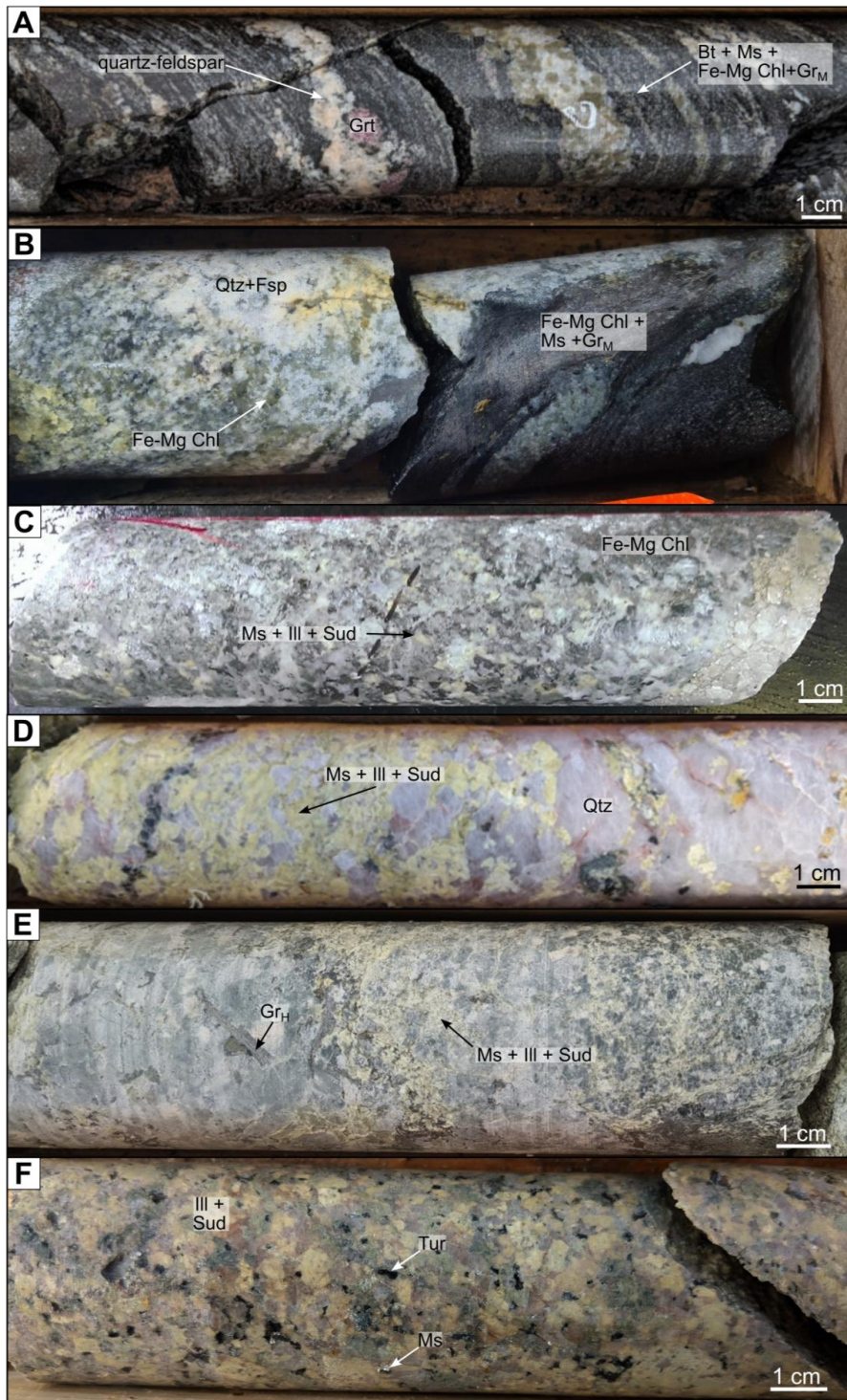
245 Figure 1: (A) Left: map of the Athabasca Basin (Saskatchewan, Canada) with the outline of the different lithotectonic
 246 units forming the basement. Right: zoom of the study area located in the eastern part of the Athabasca Basin along the
 247 WMTZ. The red lines represent “graphitic conductors” interpreted from airborne EM-surveys, which correspond to graphitic-rich shear zones
 248 hosting uranium mineralization. The yellow squares represent deposits or mineralizations with economic potential, and
 249 the blue stars represent the studied sites. Data source: Saskatchewan Geological Survey (electromagnetic data).
 250 Map created using ArcGIS Pro. (B) Schematic cross-section through the main ore body of Cigar Lake, archetype of
 251 unconformity-related U deposits. U is located at the unconformity above a ductile-brittle graphitic shear zone (Modified
 252 after Martz et al., 2019a) and is associated with an alteration halo dominated by illite and sudoite in both basin and
 253 basement. The theoretical locations of the four types of samples examined in this study are indicated by colored stars.
 254

255 **3. Materials and methods**

256 **3.1. Sampling strategy**



257 Four study areas located in the northeastern segment of the Wollaston-Mudjatik Transition Zone (WMTZ) were
258 selected to evaluate the applicability of in-situ Rb-Sr geochronology to date the main hydrothermal alteration
259 (illite-sudoite) associated with the U mineralisation within the basement rocks. From north to south, these areas
260 comprise the Waterfound (WF) and McClean South (MCS) prospects, and the Cigar Lake (CL) and McArthur
261 River (MAC) deposits. All samples from WF, MCS, and CL analyzed in this study were obtained from drill cores
262 collected during the past five years as part of U exploration programs conducted by Orano Canada Inc., whereas
263 samples from MAC were provided by Cameco Corporation. The sampling strategy at the four study sites was
264 designed to ensure both lateral and vertical representativeness, spanning from unaltered basement zones (Fig. 2A,
265 B) to hydrothermally altered domains characterized by illite-sudoite assemblages associated with the
266 mineralization (Fig. 2C, D, E, F). For MCS, five drill holes were considered from west to east: MCS-03, MCS-05,
267 MCS-34, MCS-35C and MCS-31 (mineralized conductor). For WF, six drill holes were considered from southwest
268 to northeast: WF-93, WF-98, WF-66, WF-77 and WF-75 (mineralized conductor) and WF-100 (outside the La
269 Roque Conductive Corridor). For CL, two drill holes were considered from west to east: WC-449 (mineralized
270 conductor) and WC-473 (non-mineralized conductor). For MAC, five drill holes were considered from west to
271 east: MC-408, MC-408-01, MC-418, MC-410-01, MC-410-02 (mineralized conductor). Pelitic gneisses and
272 anatetic granitoids represent the two dominant lithologies within the WMTZ, particularly within the graphite-rich
273 shear zones that host mineralization, which justifies their selection for this study. Across all investigated sites, four
274 samples of pelitic gneisses unaffected by illite-sudoite alteration were analyzed, together with five samples of
275 anatetic granitoids and/or associated leucosomes that were likewise preserved from this alteration. Their altered
276 equivalents comprise ten samples of pelitic gneisses affected by illite-sudoite alteration and nineteen samples of
277 anatetic granitoids and/or leucosomes exhibiting the same alteration signature. All samples were specifically
278 selected based on their high muscovite modal abundances and the presence of muscovite grains of sufficient size
279 to enable *in situ* Rb-Sr analyses by LA-ICP-MS.





281 **Figure 2. Macroscopic pictures of drill cores intervals sampled for this study** (A) Anatectic pelitic gneiss containing
282 metamorphic graphite (GrM), biotite (Bt), muscovite (Ms) and Fe-Mg chlorite (Fe-Mg Chl) within the restite; the
283 contact between the quartz-feldspar leucosome (Qtz+Fsp) and the restite is marked by garnet. Evidence of retro-
284 metamorphic alteration is visible within the quartz-feldspar leucosome and is characterized by a fir-green coloration
285 [MC-408_591.3 m]. (B) Anatectic pelitic gneiss showing an accumulation of metamorphic graphite in the restite; the
286 quartz-feldspar leucosome exhibits retro-metamorphic alteration features, with Fe-Mg chlorite imparting a dark green
287 coloration to the core rock [MCS-05_285.5 m]. The restite is composed of metamorphic graphite, biotite, muscovite. (C)
288 Strongly altered granitoid characterized by nearly complete replacement of feldspars and plagioclase by illite and
289 sudoite (III+Sud), while quartz and ferromagnesian chlorites remain preserved. Here, muscovite is embedded within
290 the illite-sudoite assemblage and is not macroscopically observable [WC-449_434.4 m]. (D) Granitoid exhibiting
291 pervasive illite-sudoite alteration, within which muscovite is entirely incorporated into the fine-grained alteration
292 matrix and is not discernible at the macroscopic scale [MC-410-02_687.4 m]. (E) Anatectic pelitic gneiss hosting
293 hydrothermal graphite concentrations within the leucosome, associated with the retrograde metamorphic features and
294 an illite-sudoite alteration matrix in which muscovite is cryptic and not macroscopically distinguishable. [MCS-34_273.7
295 m]. (F) Granitoid exhibiting intense illite-sudoite alteration of primary minerals, imparting an apple-green coloration
296 to the entire drill core, with muscovite and tourmaline also locally preserved and macroscopically visible [WF-93_581].

297 **3.2. Methods**

298 Scanning electron microscopy (SEM), electron probe microanalysis (EPMA), and micro-X-ray fluorescence
299 (μ XRF) analyses were performed at the Service Commun de Microscopies Électronique et de Microanalyse X
300 (SCMEM) in Nancy, France, whereas *in situ* Rb-Sr isotopic analyses were carried out on the ICP platform at
301 GeoRessources, Université de Lorraine (Nancy, France).

302 **3.2.1. Petrography - Optical and SEM**

303 Samples were first observed using a conventional optical microscope under transmitted light. Thin-section scale
304 mapping was conducted using a Keyence VHX-2000 optical microscope. Muscovite and associated minerals were
305 imaged using a TESCAN VEGA 3 LM scanning electron microscope (SEM). This SEM is equipped with a
306 conventional tungsten filament and is coupled to two Bruker XFlash 6-30 mm² EDS detectors. The backscattered
307 electron (BSE) images were obtained using the following parameters: an accelerating voltage of 15 kV, a working
308 distance (WD) of 15 mm, a beam current of 0.5 nA, and an acquisition speed of 1 ms per pixel.

309 **3.2.2. X-ray fluorescence (XRF)**

310 Thin sections were analyzed using a BRUKER M4 TORNADO micro-XRF, which enables localized analysis of
311 elements ranging from sodium to uranium, with a maximum spatial resolution of approximately 20 μ m and a
312 sensitivity varying from around one percent for light elements (Na) to several tens of ppm for more sensitive
313 elements (Zr). The device is equipped with a rhodium X-ray tube, polycapillary optics to focus the beam and two
314 Bruker SDD-type EDS detectors to enhance acquisition speed, allow for the identification of diffraction peaks,
315 and reduce shadowing effects. Mapping parameters included a 35 μ m step size, with a dwell time of 10 ms,
316 corresponding to a scan speed of 3.5 mm/s. X-ray tube parameters were set to 400 μ A and 50 kV, under a 20 mbar
317 vacuum. μ -XRF data were subsequently processed using the M4 TORNADO software to generate elemental maps.

318 **3.2.3. Electron probe microanalysis (EPMA)**

319 X-ray elemental maps of K (K α), Rb (K α), Mg (K α), Al (K α), Ca (K α), F (K α), Fe (K α), Mn (K α) and Na (K α)
320 on selected areas in thin sections were carried out using a CAMECA SX5 TACTIS electron microprobe, equipped
321 with a LaB₆ tip and five vertical WDS spectrometers. The analytical conditions included a beam current of 100
322 nA, an accelerating voltage of 25 kV, and a counting time of 20 ms per pixel.

323 **3.2.4. In situ Rb-Sr isotopic analysis (LA-ICP-MS/MS)**

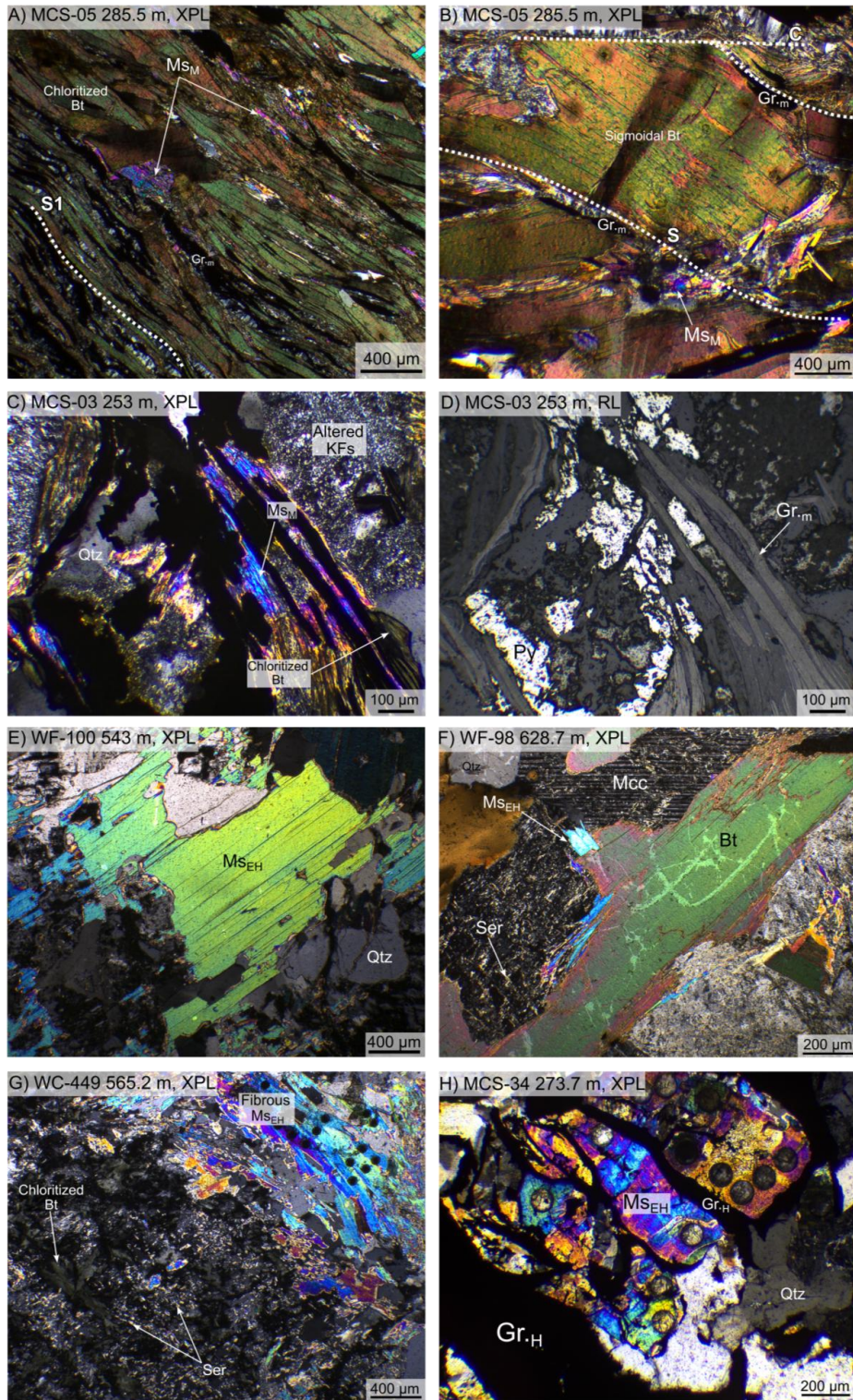


324 *In situ* Rb-Sr analyses on muscovite were carried out using a LA-ICP-MS/MS system. The $^{87}\text{Rb}/^{86}\text{Sr}$ and $^{87}\text{Sr}/^{86}\text{Sr}$
325 ratios of the studied samples and reference materials were determined using an Agilent 8900 ICP-QQQ coupled
326 with a 193 nm ArF excimer laser ablation system ESI 193 nm ArF with a TwoVol2 dual-volume ablation cell. All
327 samples were ablated employing a 50 μm spot size for 90 to 110 s (30 to 40 s of gas blank measurement and 30 to
328 40 s of ablation time followed by 30 s of sample washout), with a repetition rate of 10 Hz and a laser energy density
329 of 6 J.cm^{-2} . Helium at a flow rate of 700 $\text{mL}\cdot\text{min}^{-1}$ was used as a carrier gas in the ablation cell, then mixed with
330 N_2 via a Y connector at a flow rate of 4 mL min^{-1} and argon nebulization gas at a flow rate of 700 mL min^{-1} before
331 entering the ICP-MS torch. The reaction gas N_2O was used to overcome isobaric interferences to separate ^{87}Sr
332 from ^{87}Rb due to the efficiency of N_2O in reacting with Sr^+ to form SrO^+ ions, which was not the case for Rb^+ .
333 The following isotopes were measured (integration time in parentheses): $^{28}\text{Si} \rightarrow ^{28}\text{Si}$ (2 ms), $^{84}\text{Sr} \rightarrow ^{84}\text{Sr}$ (5 ms),
334 $^{84}\text{Sr} \rightarrow ^{100}\text{SrO}$ (120 ms), $^{85}\text{Rb} \rightarrow ^{85}\text{Rb}$ (20 ms), $^{85}\text{Rb} \rightarrow ^{101}\text{Rb}$ (5 ms), $^{86}\text{Sr} \rightarrow ^{86}\text{Sr}$ (5 ms), $^{86}\text{Sr} \rightarrow ^{102}\text{SrO}$ (120 ms),
335 $^{87}\text{Sr} \rightarrow ^{87}\text{Sr}$ (5 ms), $^{87}\text{Sr} \rightarrow ^{103}\text{SrO}$ (120 ms), $^{88}\text{Sr} \rightarrow ^{88}\text{Sr}$ (5 ms), $^{88}\text{Sr} \rightarrow ^{104}\text{SrO}$ (120 ms). A scan of all isotopes
336 (sampling period) took approximately 565 ms. Seven sessions were conducted to analyze all samples. The NIST
337 SRM 610 glass (Woodhead and Herget, 2001) and MicaMg mica (Hogmalm et al., 2017, Jegal et al., 2022) were
338 used as external standards for the correction of the $^{87}\text{Sr}/^{86}\text{Sr}$ and $^{87}\text{Rb}/^{86}\text{Sr}$ ratios, respectively. La Posta biotite was
339 used as a secondary reference material, with a reported weighted mean age of 91.6 ± 1.2 Ma (Zack and Hogmalm,
340 2016), to verify the instrumental and analytical conditions. LA-ICPMS/MS data were processed using the Iolite
341 4 software (Paton et al., 2011). The processed and calibrated data for $^{87}\text{Sr}/^{86}\text{Sr}$ and $^{87}\text{Rb}/^{86}\text{Sr}$ ratios were plotted in
342 conventional isochron and radial plots and used to calculate Rb-Sr isochron ages and corresponding regression
343 intercepts using IsoplotR (Vermeesch, 2018). In the following, regression intercepts refer strictly to the
344 mathematical intercepts of Rb-Sr regressions and are not interpreted as true initial $^{87}\text{Sr}/^{86}\text{Sr}$ ratios.

345 **4. Results**

346 Two types of muscovite, identified in the least altered zones of the metasomatic halos, were investigated (Fig. 2A
347 and B): (i) (retro-)metamorphic muscovite associated with the retrograde mineral assemblage within metamorphic
348 rocks and (ii) early hydrothermal muscovite within magmatic rocks as a secondary phase. All of the studied
349 samples exhibit evidence of a first alteration associated with the retrograde metamorphism and are variably
350 overprinted by a second hydrothermal alteration that is described below.

351





353 **Figure 3. (A-B) Graphitic pelitic gneiss [MCS-05_285.5 m]. (A) Pelitic gneiss displaying a well-developed foliation.**
354 **Biotite (Bt) and thick flakes of metamorphic graphite (Grm) are aligned along the S1 foliation, while retrograde**
355 **metamorphic muscovite (Msm) crystallizes at the rims of biotite, perpendicular to S1. (B) Plastically deformed biotite**
356 **marking a C-S fabric, with fine-grained metamorphic muscovite precipitating around biotite and within biotite pressure**
357 **shadows. (C-D) Graphitic pelitic gneiss with retrograde mineral assemblage [MCS-03_253 m]. Assemblage of quartz**
358 **(Qtz), K-feldspar (KFs), metamorphic muscovite, pyrite (Py), and metamorphic graphite, together that has undergone**
359 **chloritization related to retrograde metamorphic alteration. Metamorphic muscovite is aligned with tabular flakes of**
360 **metamorphic graphite. (E-F) Granitoid rocks [WF-100_543 m]. (E) Subhedral early hydrothermal muscovite (MSeH)**
361 **crystals. (F) Assemblage of biotite, quartz, and microcline (Mcc), showing early stages of sericitization (Ser). Early**
362 **hydrothermal muscovite precipitated as a secondary phase along biotite grain boundaries and has locally replaced, now**
363 **altered and sericitized K-feldspar [WF-98_628.7 m]. (G) Leucosome of metapelitic gneiss characterized by fibrous**
364 **aggregates of early hydrothermal muscovite crosscutting partially to completely chloritized biotite [WC-449_565.2 m].**
365 **(H) Leucosome of metapelitic gneiss with early hydrothermal muscovite associated with large flakes of hydrothermal**
366 **graphite (GrH) [MCS-34_273.7 m].**

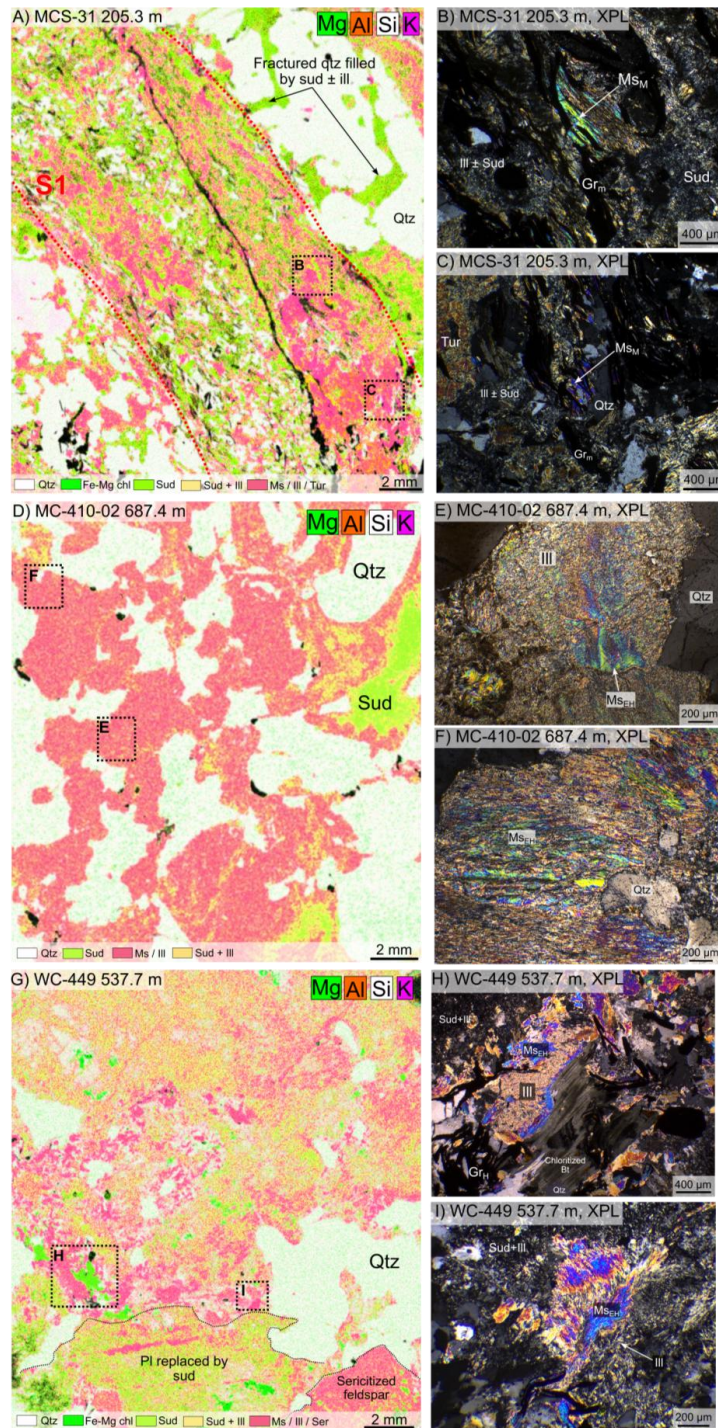
367 **4.1. Metamorphic muscovite**

368 Metamorphic muscovite is exclusively developed along the foliation planes of Paleoproterozoic metapelites (Fig.
369 2A,B) (e.g., Schneider et al., 2007; Skipton et al., 2016; Jeanneret et al., 2017; Martz et al., 2017). These rocks are
370 characterized by quartz and sericitized K-feldspar, and are bounded by graphite-rich shear zones containing biotite,
371 muscovite, and pyrite (Fig. 3A). Biotite occurs as lath-shaped crystals, locally plastically deformed showing C-S
372 planes, ranging from 0.5 to 1 mm in length, and oriented parallel to the subvertical S1 foliation. Muscovite is
373 present as euhedral to subhedral crystals, predominantly crystallizing along the rims of metamorphic biotite, with
374 an orientation perpendicular to the S1 foliation, suggesting a crystallization stage postdating biotite growth
375 possibly along the retrograde P-T path (Fig. 3A). Muscovite is also present within pressure shadows around biotite
376 mica-fish, suggesting that muscovite crystallization was contemporaneous with ductile deformation (Fig. 3B).
377 Metamorphic biotites are locally pseudomorphosed by Fe-Mg chlorite, a marker of retrograde metamorphism or
378 fluid-induced alteration (Fig. 3C). The metamorphic muscovite is commonly associated with medium-sized,
379 euhedral to tabular flakes of metamorphic graphite aligned along the foliation. Sulfides such as pyrite and
380 chalcopyrite are frequently associated with this metamorphic graphite (Fig. 3D).

381 **4.2. Early hydrothermal muscovite**

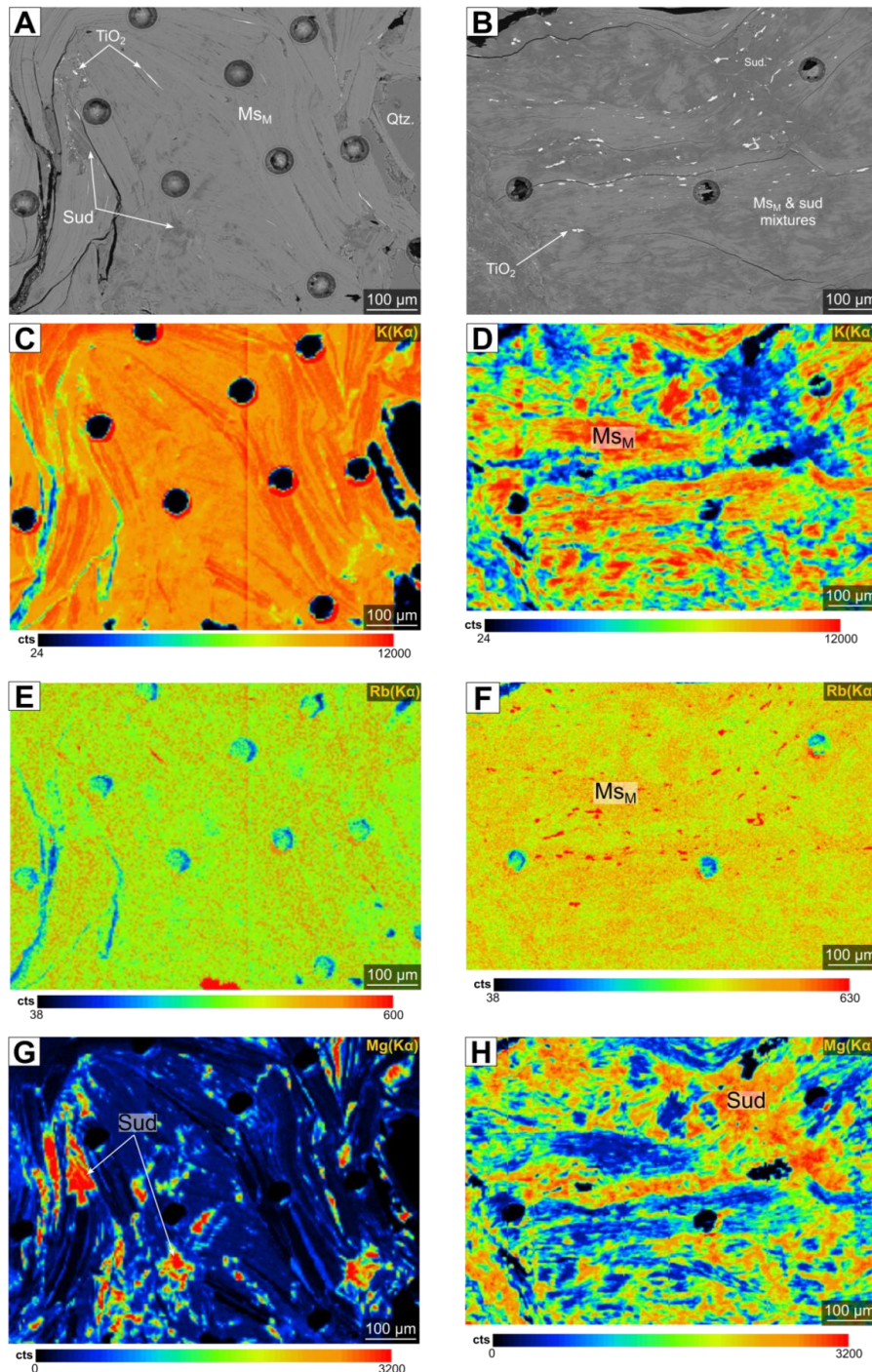
382 Early hydrothermal muscovite occurs within anatetic granitoids or within the leucosomes of metapelitic gneisses
383 (Fig. 2C, D, E, F) (e.g., Schneider et al., 2007; Skipton et al., 2016; Martz., 2017; Obin, 2025). These lithologies
384 are primarily composed of quartz, K-feldspar of the microcline type, often altered to sericite forming very fine
385 microlamellar aggregates with a shimmering whitish-grey appearance, plagioclase, and biotite laths, which are
386 partially to completely pseudomorphosed by Fe-Mg chlorite (Fig. 3E, F). Muscovite in these rocks occurs either
387 as subhedral crystals or as fibrous aggregates that may have partially to completely replaced chloritized biotite or
388 have precipitated along biotite grain boundaries as fine-grained crystals (Fig. 3E, F, G). It may also have locally
389 replaced K-feldspar (Fig. 3F). Muscovite is frequently associated with hydrothermal graphite, which occurs as
390 large flakes (up to 0.5 cm) precipitating interlayered with muscovite within late fractures or forming radiating
391 patterns in granitic leucosomes (Fig. 3H). These lithologies may also be locally enriched in tourmaline, occurring
392 as euhedral to subhedral crystals with strong relief and second-order yellow to green interference colors. Accessory
393 phases include zircon, monazite, and apatite, present as subhedral crystals or as veinlets crosscutting the
394 aforementioned minerals.

395 **4.3. Petrographic characteristics of altered muscovites**





397 **Figure 4.** (A) Micro-X-ray fluorescence (μ -XRF) elemental maps of a thin section showing the distribution of Mg, Al, Si,
398 and K within a migmatitic graphitic pelitic gneiss including a leucosome [MCS-31_205.3 m]. Illite (III)-sudoite (Sud)
399 alteration is hosted along the mylonitic foliation planes of pelitic gneisses and occurs pervasively within the leucosome.
400 Sudoite also precipitates within fractures crosscutting the quartz vein. (B-C) Magnified views of (A) showing illite-
401 sudoite alteration affecting metamorphic muscovite (Ms_m). (D) μ -XRF elemental mapping displaying the Mg, Al, Si,
402 and K distribution within an anatectic granitoid [MC-410-02_687.4 m]. Illite/sudoite ratios vary across the sample, with
403 domains that are fully illitized and others enriched in sudoite. (E-F) Magnified views of (D) illustrating the illitization
404 of early hydrothermal muscovite (Ms_{eh}). (G) μ -XRF elemental maps showing the Mg, Al, Si, and K distribution within
405 an anatectic granitoid [WC-449_537.7 m]. Illite and sudoite crystallize pervasively, with spatial variations in the
406 illite/sudoite ratio. (H-I) Magnified views of (G) showing early hydrothermal muscovite illitization and the coexistence
407 of illite-sudoite replacing early minerals. Biotite associated with early hydrothermal muscovite is completely chloritized.
408 This hydrothermal alteration affects both metamorphic muscovite (Figs. 4A-C) and early hydrothermal muscovite
409 (Figs. 4D-I). This Mg-K-type alteration pervasively affects the two lithologies that constitute the graphite-rich
410 shear zones, whether through the mylonitic foliation planes of pelitic gneisses (Figs. 4A-C), the grain boundaries
411 of magmatic to early hydrothermal minerals in anatectic granitoids and leucosomes (Figs. 4D-I), or through
412 fracture networks indiscriminately crosscutting the two lithologies. At the microscopic scale, this alteration is
413 expressed by the extensive replacement of primary and retro-metamorphic minerals by a clay assemblage
414 predominantly composed of micrometric illite, spatially associated with sudoite (a magnesium-rich trioctahedral
415 chlorite). However, this alteration is not uniformly distributed within the different lithologies, and the illite/sudoite
416 ratio varies between lithologies and within the same lithology (Figs. 4D, G). In anatectic granitoids and
417 leucosomes, the alteration is marked by the partial replacement of K-feldspar and the complete replacement of
418 plagioclase, which are more prone to alteration, by this clay assemblage (Figs. 4D-I). Fractures crosscutting quartz
419 and feldspars are commonly filled with illite and/or sudoite crystals (Fig. 4A). The cleavage planes of muscovite
420 are partially to completely disrupted, and their birefringence colors approach those of illite, reflecting the onset of
421 muscovite illitization, particularly visible along grain margins (Figs. 4E, F, H, I). Under cross-polarized light, illite
422 occurs as lath-shaped crystals (Figs. 4E, F, H, I). Sudoite appears as needle-like crystals with low relief, generally
423 $<2 \mu\text{m}$ in length (Figs. 4B, C, H, I). Figure 5 highlights the effect of illite-sudoite alteration within a single sample
424 (MC-410-01, 677.9 m), comparing a relatively preserved zone showing the onset of alteration (Fig. 5A) with a
425 fully altered zone (Fig. 5B). Backscattered electron (BSE) images reveal that in the least altered area, muscovite
426 retains its characteristic cleavage planes (Fig. 5A), whereas in the most altered area, muscovite has completely lost
427 its original morphology and is replaced by sudoite \pm illite. Mixtures of these two phases can be distinguished
428 through grayscale contrast variations (Fig. 5B). Elemental X-ray maps obtained by EPMA further emphasize these
429 mineralogical and chemical transformations (Fig. 5C-H). In the least altered zone, muscovite exhibits variable K
430 ($\text{K}\alpha$) intensities, with maximum values in the most preserved domains and progressively decreasing intensities in
431 areas showing incipient alteration (Fig. 5C). The Rb ($\text{K}\alpha$) signal follows a similar pattern, reaching its highest
432 values in the K-rich zones (Fig. 5E). This decrease in K and Rb intensities correlates with the occurrence of Mg
433 ($\text{K}\alpha$)-rich areas associated with sudoite formation along fracture zones (Fig. 5G). In the most altered zone,
434 muscovite relics (or “ghosts”) are identified by their relatively high K ($\text{K}\alpha$) and Rb ($\text{K}\alpha$) intensities (Fig. 5D, F),
435 which are spatially anti-correlated with the Mg ($\text{K}\alpha$) signal. The latter reaches its maximum intensity within the
436 sudoite matrix that surrounds these muscovite remnants (Fig. 5H).

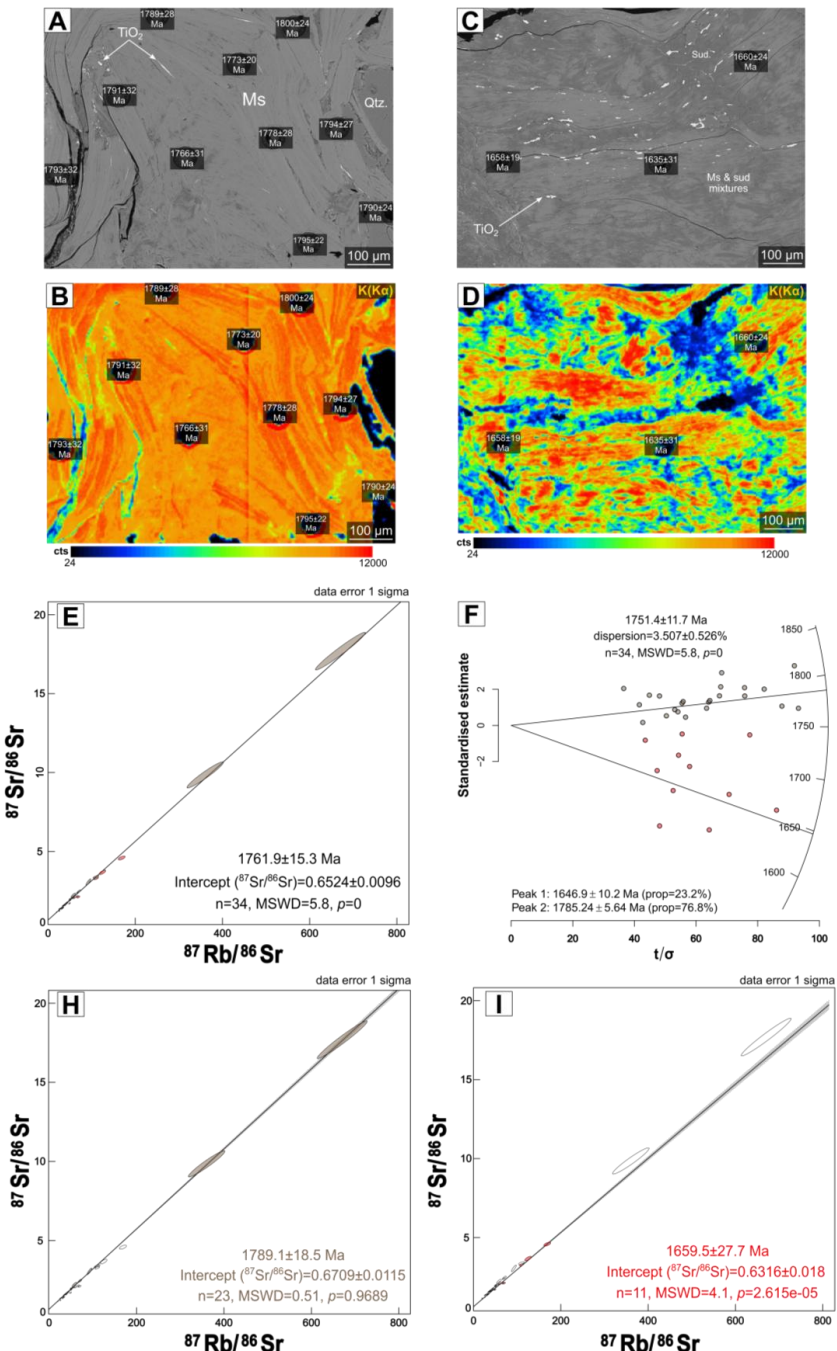




438 **Figure 5.** Two zones within the same pelitic gneiss sample [MC-410-01, 677.9 m] are shown, ranging from weakly altered
439 (A, C, E, G) to strongly altered by sudoite (B, D, F, H). (A) Preserved to partially preserved metamorphic muscovite
440 (Msm) showing the onset of alteration to sudoite along fractures, expressed by darker grey tones. (B) Strongly altered
441 metamorphic muscovite replaced by a sudoite-dominated matrix, containing very fine (<1 μ m) TiO_2 exsolution lamellae
442 that formed from the alteration of muscovite. Circular holes correspond to 50- μ m-diameter laser ablation pits. (C-D)
443 X-ray elemental maps of K (K α) for (A) and (B), respectively. (C) Gradual decrease in apparent K concentration from
444 the fully preserved zone toward the incipiently altered domain. (D) K-enriched “ghosts” of muscovite, whereas altered
445 zones are strongly to entirely depleted in K. (E-F) X-ray elemental maps of Rb (K α) acquired by EPMA for (A) and (B),
446 respectively. Apparent Rb concentration is higher in the most preserved zones in (E) and within muscovite ghosts in (D)
447 compared with illite-sudoite zones. (G-H) X-ray elemental maps of Mg (K α) acquired by EPMA for (A) and (B),
448 respectively. (G) Zones filled with sudoite are highlighted by high apparent Mg concentrations. (H) Apparent Mg
449 concentration is maximal in sudoite-rich areas and anticorrelated with the K distribution shown in (D).

450 **4.4. In situ Rb-Sr geochronology**

451 Rb-Sr isotopic analyses were performed on metamorphic and early hydrothermal muscovite sampled from both
452 unaltered and illite-sudoite-altered zones, and from the two investigated lithologies. To assess the impact of the
453 illite-sudoite alteration on the isotopic systematics of basement minerals, a representative sample of a pelitic gneiss
454 (MC-410-01, at a depth of 677.9 m) containing both well-preserved (Fig. 6A, B) and partially preserved to altered
455 muscovite grains (Fig. 6C, D) was selected for detailed *in situ* analysis by LA-ICP-MS/MS. The complete Rb-Sr
456 dataset obtained from this sample defines a Rb-Sr regression corresponding to a date of 1761.9 ± 15.3 Ma (n = 34,
457 MSWD = 5.8, p \approx 0, 1 σ), with $^{87}\text{Rb}/^{86}\text{Sr}$ ratios ranging from 19.62 to 670.44 and a corresponding $^{87}\text{Sr}/^{86}\text{Sr}$ intercept
458 of 0.6524 ± 0.0096 (Fig. 6E). The elevated MSWD value and the null probability associated with the reduced χ^2
459 test indicate significant excess scatter in the isotopic data, consistent with heterogeneous isotopic behavior at the
460 grain scale. Given this dispersion, Rb-Sr single-spot dates were calculated for each laser ablation point following
461 the approach of Rösel and Zack (2022), allowing for a direct comparison between isotopic data, petrographic
462 observations, and elemental mapping. The resulting single-spot dates display a systematic relationship with K (K α)
463 intensity maps, showing a decrease in apparent dates with decreasing K intensity, consistent with the progressive
464 alteration of muscovite (Fig. 6B, D). Radial plots illustrating the distribution of single-spot dates and isotopic ratios
465 (Galbraith, 1988, 1990; Rösel and Zack, 2022) reveal two statistically distinguishable populations with partial
466 overlap: a dominant population at 1785.2 ± 5.6 Ma (76.8%), corresponding predominantly to the least altered
467 muscovite domains, and a younger population at 1646.9 ± 10.2 Ma (23.2%), associated with increasingly altered
468 domains (Fig. 6F). When plotted separately on Rb-Sr regression diagrams, analyses from the least altered
469 muscovite domains yield a statistically robust regression corresponding to a date of 1789.1 ± 18.5 Ma (n = 23,
470 MSWD = 0.51, p = 0.9689, 1 σ), with a $^{87}\text{Sr}/^{86}\text{Sr}$ intercept of 0.6709 ± 0.0115 (Fig. 6H). In contrast, analyses from
471 the more altered and mixed domains define a less statistically reliable regression at 1659.5 ± 27.7 Ma (n = 11,
472 MSWD = 4.1, p = 2.6×10^{-5} , 1 σ), associated with a $^{87}\text{Sr}/^{86}\text{Sr}$ intercept of 0.6316 ± 0.018 (Fig. 6I). The elevated
473 MSWD values obtained for the altered domains again indicate substantial isotopic scatter. On the basis of these
474 observations and the coexistence of mixed isotopic populations within a single sample, the analytical approach
475 applied to the entire dataset, supported by petrographic and microstructural evidence, consisted of distinguishing
476 the most preserved metamorphic and early hydrothermal muscovite from those more strongly altered by an illite-
477 sudoite clay assemblage, in order to constrain the crystallization dates of these two muscovite types and the
478 potential timing(s) of alteration (Fig. 7A-E).



479

480 Figure 6. (A-D) BSE images and corresponding X-ray elemental maps of K ($\text{K}(\text{K}\alpha)$) acquired by EPMA for the pelitic gneiss sample [MC-
 481 410-01, 677.9 m] shown in Fig. 5, displaying the calculated Rb-Sr single-spot dates (Rösel and Zack, 2022) for each ablation pit. (A-B)
 482 The calculated Rb-Sr single-spot dates decrease toward zones exhibiting reduced apparent K concentrations. (C-D) The calculated Rb-



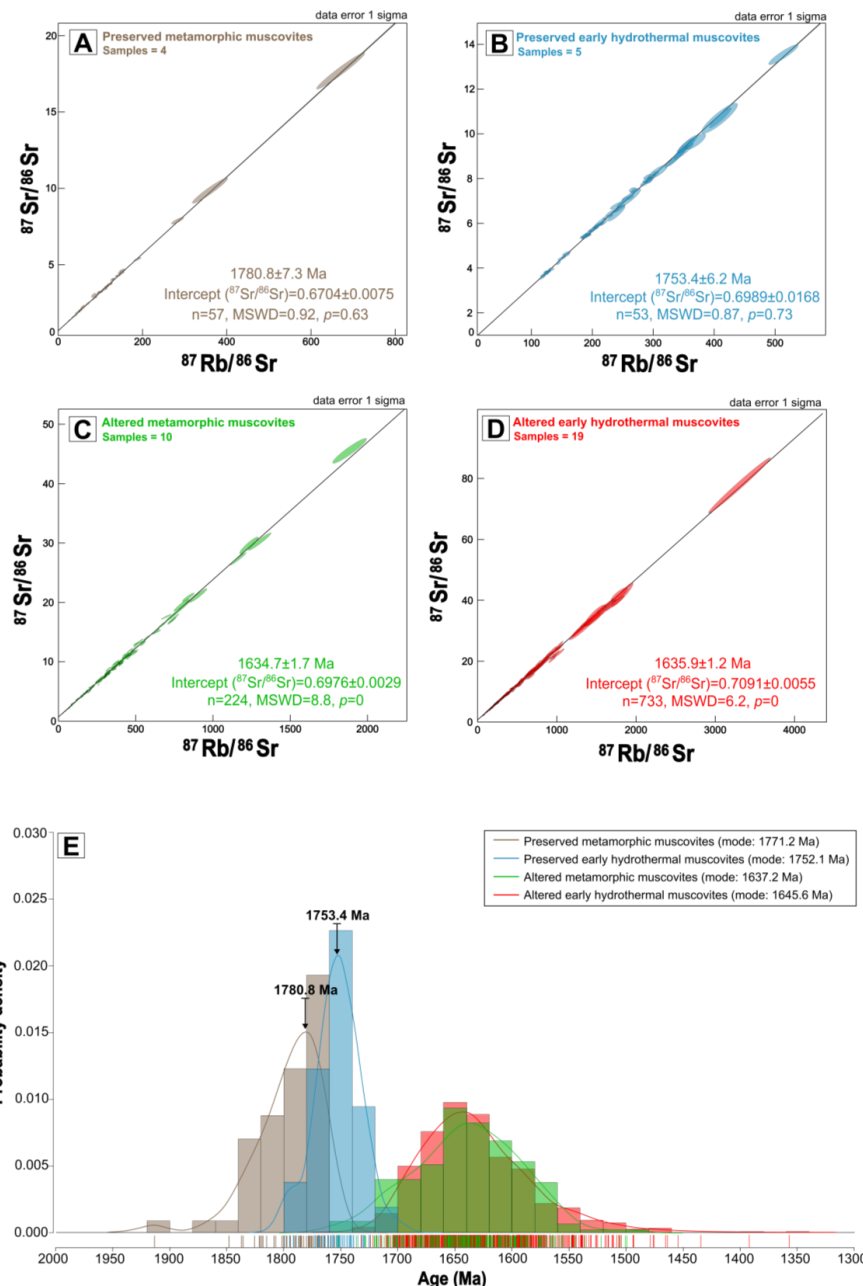
483 Sr single-spot dates are significantly younger in domains fully altered to sudoite compared to those in (A) and (B), which correspond
484 to preserved to partially preserved zones. (E) Muscovite Rb-Sr isochrons for the sample [MC-410-01, 677.9 m] obtained from both
485 preserved and altered areas. (F) Radial plot showing the dispersion of isotopic ratios and calculated single-spot dates in preserved and
486 altered domains (Galbraith, 1988, 1990; Rösel and Zack, 2022), revealing two main populations. (G) Muscovite Rb-Sr isochrons for
487 preserved domains of the sample [MC-410-01, 677.9 m]. (H) Muscovite Rb-Sr isochrons for altered domains of the same sample. Brown
488 symbols correspond to preserved muscovite, and red symbols correspond to partially to completely altered muscovite. All errors are
489 reported at 1σ .

490 4.4.1. Rb-Sr dating of metamorphic muscovite

491 The weighted mean of the Rb-Sr data obtained from all preserved metamorphic muscovite grains (four samples)
492 defines a composite Rb-Sr regression at 1780.8 ± 7.3 Ma ($n = 57$, MSWD = 0.92, $p = 0.63$, 1σ), associated with a
493 $^{87}\text{Sr}/^{86}\text{Sr}$ intercept of 0.6704 ± 0.0075 and overall $^{87}\text{Rb}/^{86}\text{Sr}$ ratios ranging from 19 to 671 (Fig. 7A). Rb-Sr single-
494 spot dates for preserved metamorphic muscovite were calculated using a fixed $^{87}\text{Sr}/^{86}\text{Sr}$ reference value of 0.6704,
495 corresponding to the intercept of the composite regression. This value is used here as an operational reference
496 parameter; owing to its low magnitude, reasonable variations in this parameter exert only a minor influence on the
497 calculated dates, as previously demonstrated by Rösel and Zack (2022). The resulting single-spot dates range from
498 1760 ± 15 Ma to 1914 ± 44 Ma and define a single statistically coherent population with a modal value of 1771.2
499 Ma (Fig. 7E). Matrix-corrected elemental concentrations (using an applied correction factor of 0.532038) range
500 from 33 to 145 ppm (average: 81 ppm) for ^{87}Rb , from 0.19 to 2.46 ppm (average: 1.03 ppm) for ^{86}Sr , and from
501 1.28 to 4.50 ppm (average: 2.73 ppm) for ^{87}Sr .

502 4.4.2. Rb-Sr dating of early hydrothermal muscovite

503 The weighted mean of the Rb-Sr data obtained from preserved early hydrothermal muscovite (five samples)
504 defines a composite regression at 1753.4 ± 6.2 Ma ($n = 53$, MSWD = 0.87, $p = 0.73$, 1σ), associated with a $^{87}\text{Sr}/^{86}\text{Sr}$
505 intercept of 0.6989 ± 0.0168 and overall $^{87}\text{Rb}/^{86}\text{Sr}$ ratios ranging from 34 to 514 (Fig. 7B). Rb-Sr single-spot dates
506 for preserved early hydrothermal muscovite were calculated using the same fixed $^{87}\text{Sr}/^{86}\text{Sr}$ reference value of
507 0.6704, which has a negligible influence on the resulting dates (e.g., Rösel and Zack, 2022). The calculated single-
508 spot dates span from 1701.9 ± 28.8 Ma to 1799.5 ± 21.4 Ma and cluster into a single statistically consistent
509 population with a modal value of 1752.1 Ma (Fig. 7E). Matrix-corrected elemental concentrations (using an
510 applied correction factor of 0.532038) range from 60.5 to 144.7 ppm (average: 111.3 ppm) for ^{87}Rb , from 0.22 to
511 2.26 ppm (average: 0.55 ppm) for ^{86}Sr , and from 1.82 to 3.97 ppm (average: 3.15 ppm) for ^{87}Sr .



512

513 **Figure 7. (A) Rb-Sr isochrons for metamorphic muscovite preserved from illite-sudoite alteration, represented by four samples. (B)**
 514 **Rb-Sr isochrons for early hydrothermal muscovite preserved from illite-sudoite alteration, represented by five samples. (C) Rb-Sr**
 515 **isochrons for metamorphic muscovite affected by illite-sudoite alteration, represented by ten samples. (D) Rb-Sr isochrons for early**
 516 **hydrothermal muscovite affected by illite-sudoite alteration, represented by nineteen samples. (E) Density diagram constructed from**
 517 **individual single-spot dates obtained for preserved metamorphic muscovite (brown), preserved early hydrothermal muscovite (blue),**
 518 **illite-sudoite altered metamorphic muscovite (dark red), and illite-sudoite altered early hydrothermal muscovite (red). A bin width of**



519 **20 Ma was used for the histogram. The isochron dates calculated in (A) and (B) are indicated by bold arrows for the preserved**
520 **metamorphic and early hydrothermal muscovite.**

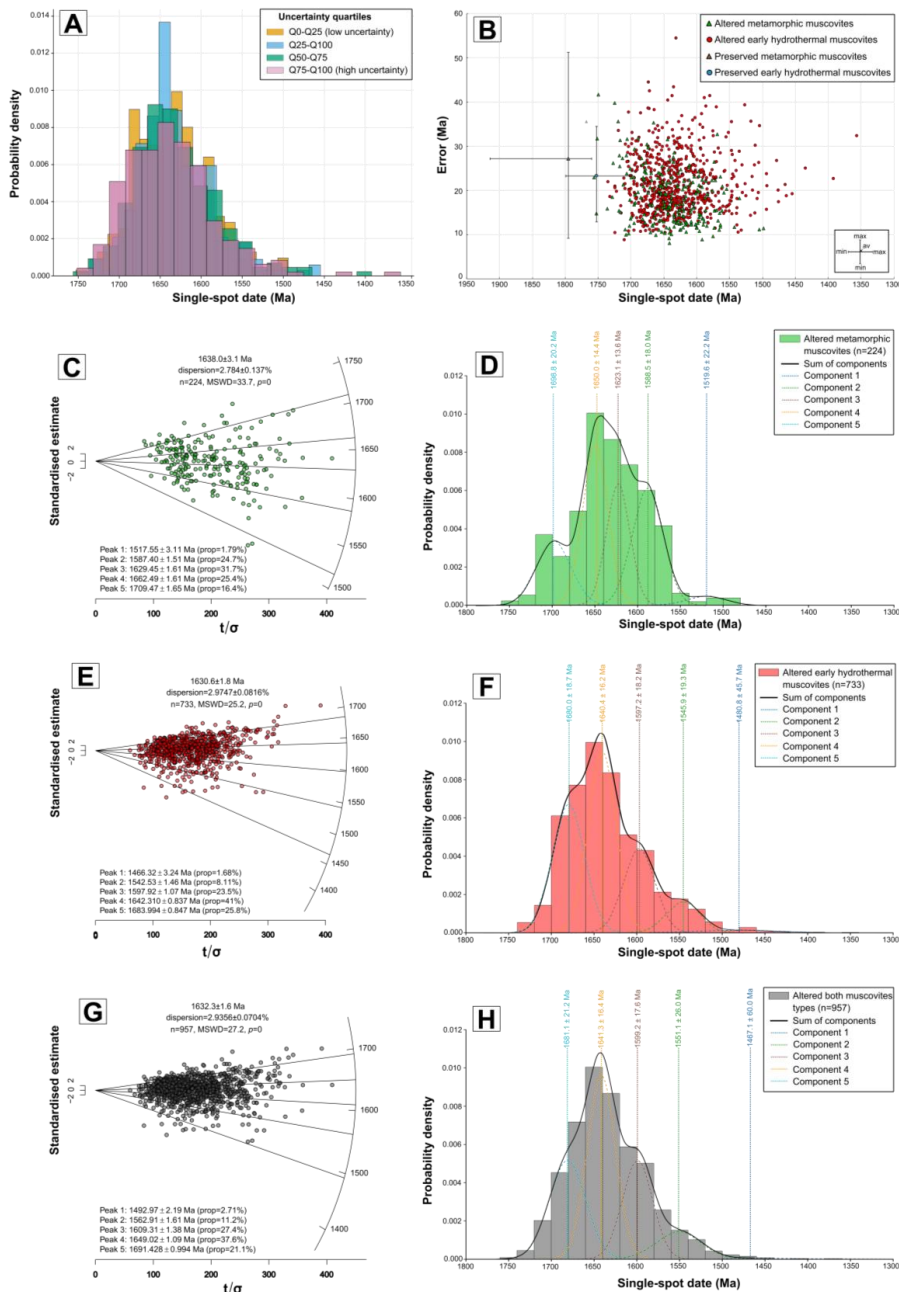
521 **4.4.3. Rb-Sr dating of altered muscovites**

522 The weighted mean of the dates obtained for the metamorphic muscovite affected by illite-sudoite hydrothermal
523 alteration defines regressions at 1634.7 ± 1.7 Ma for metamorphic muscovite (ten samples, $n = 224$, MSWD = 8.8,
524 $p = 0$, 1σ) and at 1635.9 ± 1.2 Ma for early hydrothermal muscovite (nineteen samples, $n = 733$, MSWD = 6.2, p
525 = 0, 1σ), associated with $^{87}\text{Sr}/^{86}\text{Sr}$ intercepts of 0.6976 ± 0.0029 and 0.7091 ± 0.0055 , respectively (Fig. 7C, D).
526 The elevated MSWD values and null probabilities indicate significant excess scatter in both datasets for both
527 muscovite types. Single-spot Rb-Sr dates obtained from altered muscovite display a broad and erratic distribution,
528 ranging from 1498.6 ± 11.4 Ma to 1756.2 ± 22.9 Ma (modal value of 1637.2 Ma) for metamorphic muscovite, and
529 from 1357.0 ± 32.4 Ma to 1735.1 ± 21.9 Ma (modal value of 1645.6 Ma) for early hydrothermal muscovite (Fig.
530 7E). Matrix-effect-corrected concentrations (using and applied correction factor of 0.532038) for the metamorphic
531 muscovite range from 21.7 to 213.6 ppm (mean: 99.9 ppm) for ^{87}Rb , from 0.10 to 3.74 ppm (mean: 0.62 ppm) for
532 ^{86}Sr , and from 0.9 to 5.8 ppm (mean: 2.76 ppm) for ^{87}Sr . Matrix-effect-corrected concentrations for the early
533 hydrothermal muscovite range from 9.18 to 3222.9 ppm (mean: 190.4 ppm) for ^{87}Rb , from 0.05 to 15.8 ppm (mean:
534 0.82 ppm) for ^{86}Sr , and from 0.44 to 75.4 ppm (mean: 4.95 ppm) for ^{87}Sr .

535 The analysis of calculated single-spot Rb-Sr dates as a function of uncertainty quartiles reveals an overall
536 homogeneous distribution, with moderate variations in central values and dispersion across uncertainty levels (Fig.
537 8A). The dataset was divided into four groups corresponding to the uncertainty quartiles (Q0-Q25, Q25-Q50, Q50-
538 Q75, and Q75-Q100). The group with the lowest uncertainty (Q0-Q25) comprises 241 observations, yielding a
539 mean date of 1633.3 Ma ($\sigma = 45.3$ Ma). The second quartile (Q25-Q50) includes 239 samples, with a mean date
540 of 1630.7 Ma ($\sigma = 44$ Ma). In the third quartile (Q50-Q75), the mean remains stable at 1630.6 Ma, although the
541 standard deviation increases slightly ($\sigma = 51.5$ Ma), reflecting greater variability. Finally, the quartile with the
542 highest uncertainty (Q75-Q100) encompasses 239 data points, showing a slightly higher mean date (1637.2 Ma)
543 and the greatest dispersion ($\sigma = 53.9$ Ma). Examination of the minimum and maximum values indicates a gradual
544 broadening of the single-spot Rb-Sr date distribution with increasing uncertainty, ranging from 1493.8 to 1752.7
545 Ma in the first quartile to 1357.0 to 1751.5 Ma in the last. This trend suggests that measurements associated with
546 higher uncertainties encompass a wider range of dates (Fig. 8B). Overall, the normalized single-spot date
547 distributions by quartile display relatively similar patterns, indicating no major bias related to analytical
548 uncertainty, although a slight increase in variability is observed. This observation highlights that, while individual
549 uncertainties do not significantly affect the mean of the single-spot dates, they are associated with greater
550 dispersion in the extreme values. To address the heterogeneous distribution of single-spot dates and the variability
551 of their individual uncertainties, a statistical approach based on a Gaussian Mixture Model (GMM) was applied
552 (McLachlan and Peel, 2000; Melnykov and Melnykov, 2012; Glodek et al., 2013; Nguyen and McLachlan, 2015;
553 McLachlan et al., 2019). The GMM, applied to the logarithmically transformed Rb-Sr single-spot dates of both
554 muscovite types, enables the decomposition of the overall dataset into multiple components characterized by
555 distinct probabilistic centers. A suite of GMMs with varying numbers of Gaussian components was evaluated, with
556 model performance assessed using the Bayesian Information Criterion (BIC), which balances goodness of fit
557 against model complexity. Although solutions with different numbers of components were obtained, the five-



558 component model emerged most consistently across repeated runs and is therefore presented here. This
559 configuration is compatible with the number of populations identified from IsoplotR radial plots (Galbraith, 1988,
560 1990), providing a coherent basis for methodological comparison. The GMM-derived components were
561 subsequently examined in relation to the statistically coherent clusters defined by the radial plot approach, which
562 explicitly accounts for individual analytical uncertainties. Statistical analyses conducted on the hydrothermally
563 altered muscovite show good overall consistency between the date clusters identified by the radial plots (IsoplotR)
564 and those inferred from the GMM. For altered metamorphic muscovite, the radial plot reveals five statistical
565 groupings (Fig. 8C): 1517.6 ± 3.1 Ma (1.8 % of analyses), 1587.4 ± 1.5 Ma (24.7 %), 1629.5 ± 1.6 Ma (31.7 %),
566 1662.5 ± 1.6 Ma (25.4 %), and 1709.5 ± 1.7 Ma (16.4 %). The corresponding GMM also distinguishes multiple
567 components, including a dominant one at 1650.0 ± 14.4 Ma (33.3 %), and secondary components at 1698.8 ± 20.2
568 Ma (18.9 %), 1623.1 ± 13.6 Ma (24.5 %), 1585.5 ± 18.0 Ma (21.0 %), and 1519.6 ± 22.2 Ma (2.4 %) (Fig. 8D).
569 For altered early hydrothermal muscovite, the radial plot identifies five statistical clusters (Fig. 8E): 1466.3 ± 3.2
570 Ma (1.7 % of analyses), 1542.5 ± 1.5 Ma (8.1 %), 1597.9 ± 1.1 Ma (23.5 %), 1642.3 ± 0.8 Ma (41 %), and 1684.0
571 ± 0.8 Ma (25.8 %). The corresponding GMM also resolves several components, including a main one at $1640.4 \pm$
572 16.2 Ma (38.4 %), and secondary components at 1680.0 ± 18.7 Ma (31.7 %), 1597.2 ± 18.2 Ma (19.7 %), 1545.9
573 ± 19.3 Ma (8.1 %), and 1480.8 ± 45.7 Ma (1.8 %) (Fig. 8F). When combining the results for illite-sudoite zones
574 of both muscovite types, the radial plot identifies five statistical clusters (Fig. 8G): 1493.0 ± 2.2 Ma (2.7 % of
575 analyses), 1562.9 ± 1.6 Ma (11.2 %), 1609.3 ± 1.4 Ma (27.4 %), 1649.0 ± 1.1 Ma (37.6 %), and 1691.4 ± 1.0 Ma
576 (21.1 %). The corresponding GMM also distinguishes several components, including a dominant one at $1641 \pm$
577 16.4 Ma (37.6 %), and secondary components at 1681.1 ± 21.2 Ma (28.2 %), 1599.2 ± 17.6 Ma (23.7 %), $1551 \pm$
578 26 Ma (9.6 %), and 1467 ± 60 Ma (0.9 %) (Fig. 8H).



579

580 Figure 8. (A) Probability density histograms of calculated Rb-Sr single-spot dates for metamorphic and early hydrothermal muscovite
 581 affected by illite-sudoite alteration, sorted according to the quartiles of individual analytical uncertainties. The shape of the single-spot
 582 date distributions varies slightly with uncertainty level. Low uncertainties correspond to tightly clustered and homogeneous Rb-Sr
 583 single-spot dates, whereas high uncertainties are associated with greater dispersion and more pronounced asymmetry. (B) Scatter plot
 584 of analytical uncertainties versus Rb-Sr single-spot dates for altered metamorphic and early hydrothermal muscovite. For the



585 preserved metamorphic and early hydrothermal muscovites, the mean values of single-spot Rb-Sr dates and their associated analytical
586 uncertainties are reported, together with their respective maximum and minimum values. (C) Radial plot illustrating the dispersion of
587 isotopic ratios and calculated single-spot dates for altered metamorphic muscovite. Five statistical populations are identified in the
588 radial plot. (D) Gaussian mixture model (GMM) applied to log-transformed dates, representing the distribution of Rb-Sr single-spot
589 dates of altered metamorphic muscovite, weighted by their uncertainties, together with the five components identified by the GMM.
590 (E) Radial plot showing the dispersion of isotopic ratios and calculated single-spot dates for altered early hydrothermal muscovite.
591 Five statistical populations are identified. (F) Gaussian mixture model applied to log-transformed dates representing the distribution
592 of Rb-Sr single-spot dates for altered early hydrothermal muscovite, weighted by uncertainties, together with the five components
593 identified by the GMM. (G) Radial plot showing the dispersion of isotopic ratios and calculated single-spot dates for altered
594 metamorphic and early hydrothermal muscovite combined. Five statistical populations are identified. (H) Gaussian mixture model
595 applied to log-transformed dates representing the distribution of combined altered metamorphic and early hydrothermal muscovite
596 Rb-Sr single-spot dates, weighted by uncertainties, as well as the five components identified by the GMM. The components identified
597 by the GMM closely correspond to the statistical populations defined by the radial plots, taking into account the associated
598 uncertainties. A bin width of 20 Ma was used for each GMM, consistent with the average of the individual analytical uncertainties
599 calculated for each spot.

600 5. Discussion

601 5.1. Behavior of Rb and Sr and related Rb/Sr isotopic systems in muscovite from basement lithologies 602 affected by post-crystallization hydrothermalism

603 The study of basement lithologies along a gradient from non-hydrothermally altered to strongly hydrothermally
604 altered zones beneath unconformity-type uranium deposits has revealed significant mineralogical, geochemical,
605 and isotopic modifications. Across the four investigated sites, this alteration, macroscopically characterized by an
606 apple-green color affecting the foliation planes of metapelitic gneisses, leucosomes, and granitoids, as well as
607 filling fractures crosscutting the host lithologies (Figs. 2C, D, E, F and 4), manifests microscopically as the
608 progressive replacement of primary and retro-metamorphic minerals (plagioclase, K-feldspars, muscovite, biotite,
609 Fe-Mg chlorite) by an assemblage of illite and sudoite. Textural evidence suggests that these two minerals
610 crystallized synchronously or nearly synchronously (Pacquet and Weber, 1993; Percival and Kodama, 1989). This
611 alteration induces pronounced mineralogical transformations in both metamorphic and early hydrothermal
612 muscovite, involving a partial to complete breakdown of their crystal structure. This process is expressed either as
613 illitization initiated along the cleavage planes of muscovite, synchronous or quasi-synchronous with sudoite
614 precipitation, or as massive sudoite crystallization enveloping muscovite relics (Figs. 5B, 8). Illite-sudoite
615 alteration constitutes the most pervasive and intense hydrothermal alteration affecting both the Athabasca Basin
616 sandstones and the underlying basement in the vicinity of unconformity-related uranium mineralization, and has
617 long been recognized as a robust exploration vector for U deposits (e.g., Carl et al., 1992; Derome et al., 2005;
618 Cloutier et al., 2009; Ng et al., 2013; Martz, 2017; Kaczowka, 2021; Powell et al., 2022). This alteration is
619 associated with a loss of Al, Na, K and Sr and a gain in Mg, Li and B (Martz et al., 2019a). The loss of K, Na, Al
620 and Sr is easily explained by the K-feldspars and plagioclases replacement by illite plus sudoite. Part of these
621 elements remains in the system and is *in situ* transferred to the newly-formed clays whereas the rest leaves the
622 system. This process results from the circulation of marine-derived basinal brines, generated during early to middle
623 diagenesis of the sedimentary basin (Hoeve and Sibbald, 1978; Kotzer and Kyser, 1995; Kyser et al., 2000).

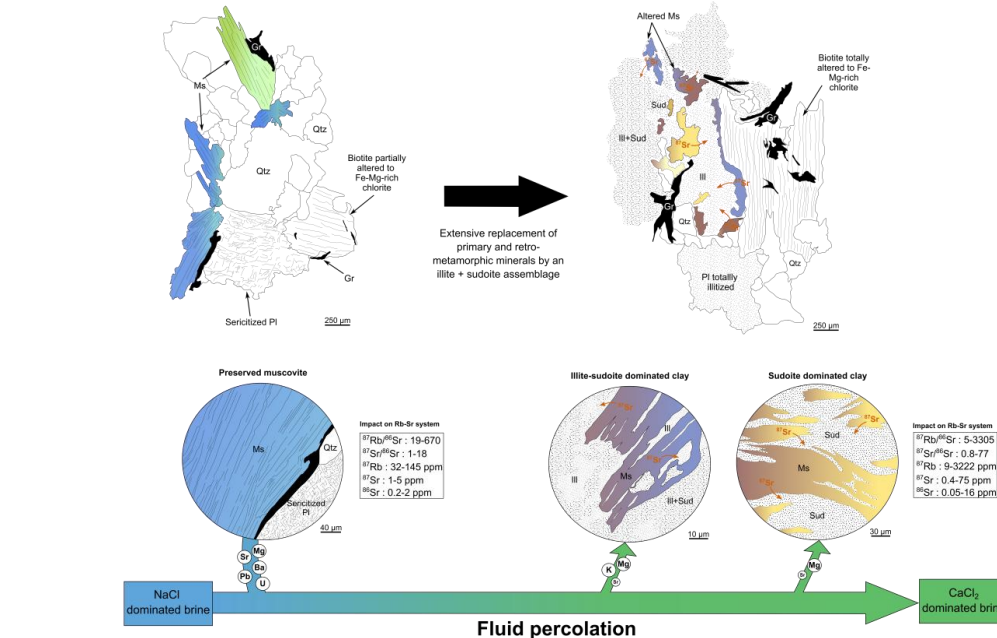
624 This illite + sudoite assemblage formed at temperatures between 150 and 220 °C, under pressures corresponding
625 approximately to the base of the sedimentary basin (ca. 1-3 kbar) (Halter, 1988; Kotzer and Kyser, 1995; Cloutier



626 et al., 2009; Martz, 2017). It is associated with important chemical modifications of the host rocks, notably the
627 loss of K, Na, Al, and Sr due to destabilization of primary feldspars and micas, and the concomitant gain in Mg,
628 Li, B, and Ca reflecting the composition of the basinal brine and its prolonged interaction with silicates. The
629 observed B and Mg enrichments are attributed to the intrinsic composition of the basinal fluid (Mercadier et al.,
630 2012; Richard et al., 2011) rather than to a local metamorphic source. Variations in the illite/sudoite ratio reflect
631 changes in thermal gradient (Beaufort et al., 2005; Kotzer and Kyser, 1995; Martz, 2017), in fluid composition
632 (Cloutier et al., 2009), notably the K^+/Mg^{2+} ratio, as well as in host rock lithology (Bruneton, 1993; Pacquet and
633 Weber, 1993; Mercadier et al., 2012; Kyser and Cuney, 2015; Martz, 2017) and system pH (Kyser et al., 2000;
634 Kister et al., 2005; Mercadier et al., 2012; Martz, 2017). The illite-sudoite alteration is not related to the
635 recrystallization of new generations of metamorphic or early hydrothermal muscovite but instead results from fluid
636 circulation that induces mineralogical, geochemical, and isotopic modifications. Isotopically, progressive
637 alteration leads to systematic variations in Rb-Sr systematics, as mineralogical transformations modify both
638 elemental concentrations and isotopic ratios. The $^{87}\text{Rb}/^{86}\text{Sr}$ ratios increase from 20-670 to 5-3305, while $^{87}\text{Sr}/^{86}\text{Sr}$
639 ratios shift from 1.18 to 1.78, with corresponding single-spot dates decreasing from 1701.9-1914.8 to 1357.0-
640 1756.2 Ma (Fig. 9). According to Dodson (1973), the loss of radiogenic ^{87}Sr controls the Rb-Sr geochronometer.
641 The observed shift in Rb-Sr systematics is primarily attributed to the partial to complete loss of radiogenic ^{87}Sr
642 from the system in response to fluid circulation associated with illite-sudoite alteration. This process results in
643 partial to complete resetting of the Rb-Sr isotopic system (Matheney et al., 1990; Kalt et al., 1994; Evans et al.,
644 1995; Eberlei et al., 2015). Elemental maps further demonstrate that Rb is also mobile; however, the mobility of
645 radiogenic ^{87}Sr is significantly greater than that of Rb and non-radiogenic Sr. This contrast in mobility accounts
646 for the observed variations in both Rb/Sr ratios and Sr isotopic compositions (Fig. 5E and F) and could explain the
647 erratic data distribution. The structural destabilization of metamorphic and early hydrothermal muscovite during
648 hydrothermal alteration, facilitated by illitization and/or sudoitization along cleavage planes, may have enhanced
649 diffusion and leaching of radiogenic ^{87}Sr . This process likely promoted the transfer of ^{87}Sr into clay phases and/or
650 the fluid phase (Fig. 9). In addition, radiogenic ^{87}Sr produced in situ may occupy transient interlayer or defect-
651 related positions that are crystallographically unfavorable for a divalent cation, whose ideal coordination
652 environment lies in octahedral sites. This crystallographic mismatch promotes diffusion of ^{87}Sr out of interfolial
653 domains typically reserved for monovalent LILEs such as K^+ or Rb^+ (e.g., Brigatti and Guggenheim, 2002). The
654 transfer of ^{87}Sr into the fluid phase could account for the Sr contents measured in brines trapped in fluid inclusions
655 (Mercadier et al., 2012; Richard et al., 2011; Martz, 2017).
656 Furthermore, the measured isotopic ratios $^{87}\text{Rb}/^{86}\text{Sr}$ and $^{87}\text{Sr}/^{86}\text{Sr}$, as well as ^{87}Rb and ^{87}Sr concentrations, are
657 significantly higher in altered muscovites than in unaltered muscovites. The simultaneous increase in $^{87}\text{Rb}/^{86}\text{Sr}$
658 and $^{87}\text{Sr}/^{86}\text{Sr}$ ratios in muscovites affected by alteration or fluid circulation reflects reopening of the Rb-Sr system
659 and selective mass redistribution of Sr during the hydrothermal event. Glodny and Grauert (2009) and Eberlei et
660 al. (2015) demonstrated that such concurrent increases do not require mica recrystallization but rather result from
661 a combination of dynamic fluid-rock interaction processes. These include: (i) a net loss of Sr through accelerated
662 diffusion along defects (microfractures, cleavage planes, subgrains, dislocations), favoring the preferential loss of
663 radiogenic Sr from transient interlayer sites or defect-related positions in muscovite; (ii) a decrease in the molar
664 fraction of Sr, which automatically increases the $^{87}\text{Rb}/^{86}\text{Sr}$ ratio since Rb is relatively immobile; and (iii) a minor



665 incorporation of Sr, possibly more radiogenic, from the matrix reservoir or from the fluid (e.g., derived from
 666 feldspar alteration) into altered muscovite, which can slightly increase the measured $^{87}\text{Sr}/^{86}\text{Sr}$ ratio.



667

668 Figure 9. Schematic representation of the effect of illite-sudoite alteration on the Rb-Sr geochronometer in basement-hosted muscovite
 669 within the context of unconformity-related uranium deposits, resulting from the percolation of a Ca-Cl_2 -dominated brine and fluid-
 670 rock interaction. This hydrothermal episode induces extensive replacement of primary and retro-metamorphic minerals by an illite-
 671 sudoite clay assemblage whose modal proportions vary among samples. The alteration fluid, which may circulate along pre-existing
 672 pathways generated during retro-metamorphic alteration of primary minerals, disrupts the crystal lattice of muscovite along cleavage
 673 planes. This structural breakdown leads to the loss of radiogenic ^{87}Sr from muscovite, which is redistributed into the fluid and/or the
 674 newly formed clay phases. Systematic fluid-inclusion studies (e.g., Mercadier et al., 2012; Richard et al., 2011; Martz, 2017) reveal that
 675 the regional brine, initially seawater-derived and NaCl -dominated, became progressively enriched in K, Sr, Mg, and B, and evolved
 676 toward a CaCl_2 -dominated composition through prolonged interaction with the host rocks. This alteration episode also results in
 677 increased Rb/Sr isotopic ratios in muscovite, together with elevated ^{87}Rb and ^{87}Sr contents, which may be explained by Sr loss from the
 678 muscovite molar fraction and by minor incorporation of Sr derived from either the rock matrix reservoir or the circulating fluid.

679 5.2. Assessing the reliability and applicability of the Rb-Sr system in metamorphic and early 680 hydrothermal muscovite

681 The characterization of well-preserved micro-domains enabled the acquisition of statistically robust isotopic ages
 682 for both the metamorphic muscovite associated with the foliation of metapelitic gneisses and the early
 683 hydrothermal muscovite from anatetic granitoids or occurring in the leucosomes of metapelitic gneisses. These
 684 muscovite grains preserved from illite-sudoite alteration define well-correlated Rb-Sr regressions yielding dates
 685 of 1780.8 ± 7.3 Ma and 1753.4 ± 6.2 Ma, respectively (Fig. 7A, B). However, the corresponding regression
 686 intercepts (0.6704 ± 0.0075 and 0.6989 ± 0.0168) fall below the minimum $^{87}\text{Sr}/^{86}\text{Sr}$ value of the solar system
 687 (~ 0.698) and therefore cannot represent physically meaningful initial isotopic compositions. These intercepts are



688 thus not interpreted as true initial $^{87}\text{Sr}/^{86}\text{Sr}$ ratios but rather as apparent values resulting from disturbed Rb-Sr
689 systematics. Low MSWD values (< 1) and high p-values ($p >> 0.05$) indicate strong internal coherence of the
690 datasets, suggesting that the regressions are statistically robust despite their anomalous intercepts. Such features
691 are characteristic of rotated or disturbed isochrons formed under open-system conditions, in which Rb and Sr are
692 redistributed in a non-conservative manner (Brooks et al., 1976; Faure and Mensing, 2013; Dickin, 2018).
693 Proportional loss of Rb relative to Sr, selective Sr mobility during fluid-rock interaction, or partial isotopic resetting
694 during metamorphism may rotate an originally valid isochron, yielding geologically reasonable slopes but non-
695 physical intercepts (Brooks et al., 1976; DePaolo, 1981; Villa, 1998; Faure and Mensing, 2013). The
696 reproducibility of measured $^{87}\text{Sr}/^{86}\text{Sr}$ ratios for the NIST SRM 610 reference material, together with the
697 consistency of the regression intercept obtained for the La Posta biotite reference material, indicates that the
698 measured $^{87}\text{Sr}/^{86}\text{Sr}$ ratios and derived regression intercepts are not attributable to analytical bias or standardization
699 issues, thereby effectively excluding an analytical or calibration-related origin. Accordingly, the anomalously low
700 intercept values are interpreted as mathematical artefacts arising from open-system Rb-Sr behavior rather than as
701 geologically meaningful isotopic signatures. In contrast, the slopes of the regressions may still record geologically
702 significant timing information related to muscovite crystallization or partial isotopic resetting, as has been
703 documented in other disturbed Rb-Sr systems (Brooks et al., 1976; Villa, 1998; Zack and Hogmalm, 2016).

704 The single-spot ages obtained from metamorphic muscovite developed along foliation planes in Paleoproterozoic
705 pelitic gneisses (e.g., Schneider et al., 2007; Skipton et al., 2016; Jeanneret et al., 2017; Martz, 2017) range from
706 1914 ± 44 Ma to 1760 ± 15 Ma, with a modal value of 1771.2 Ma and an isochrone age of 1780.8 ± 7.3 Ma (Fig.
707 10). The mean age derived from single-spot analyses, together with the isochrone age, falls within the temporal
708 window of the M2-D2 event, which generated the northeast-striking structural trend of the WMTZ and formed
709 under a sinistral transpressional tectonic regime during the late stages of the oblique Hudsonian collision, between
710 ca. 1813 and 1770 Ma (Fig. 10). Thermobarometric estimates indicate that rocks of the study area were re-
711 equilibrated under conditions of ca. 5 kbar and 750-825 °C at this time (Annesley et al., 1992, 1997a,b,c, 1999a,b;
712 Jeanneret et al., 2017; Toma et al., 2024). The M2-D2 temporal interval is supported by geochronological
713 constraints derived from other mineral phases using various U-Pb chronometers, including monazite (Pb diffusion
714 at ca. 500-800 °C; e.g., Cherniak et al., 2004; McFarlane and Harrison, 2006), zircon (>900 °C; Cherniak and
715 Watson, 2001), and titanite (500-800 °C; Kohn, 2017). The distribution of Rb-Sr single-spot ages in metamorphic
716 muscovite is shifted toward the lower limit of this time window (Fig. 10) and reflects the neoformation of
717 muscovite along the retrograde P-T path (≤ 700 °C), possibly in the presence of fluids and the cooling of
718 muscovite below the closure temperature of the Rb-Sr system, estimated at ca. 450-600 °C (Dodson, 1973). Above
719 this closure temperature, Sr diffusion remained sufficiently rapid to maintain an open isotopic system, allowing
720 equilibration with the surrounding matrix or between minerals.

721 In contrast, the single-spot ages measured in early hydrothermal muscovite crystallized within anatectic granitoids
722 or within leucosomes of metapelitic gneisses (e.g., Schneider et al., 2007; Skipton et al., 2016; Martz, 2017) range
723 from 1799.5 ± 21.4 Ma to 1701.9 ± 28.8 Ma, with a mode at 1752.1 Ma and an isochrone age of 1753.4 ± 6.2 Ma
724 (Fig. 10). The mean age derived from single-spot analyses, together with the isochrone age, falls within the temporal
725 window of the exhumation and orogenic cooling phase of the Trans-Hudsonian orogen, a period characterized by
726 the end of migmatization with the crystallization of leucosomes, the emplacement of leucogranitic intrusions, and
727 the onset of hydrothermal activity associated with the cooling phase. Although its precise duration remains poorly



728 constrained, this cooling interval is typically considered to span from ca. 1.77 Ga (750 °C, 5 kbar) to ca. 1.72 Ga
729 (350 °C, 2 kbar), as documented in several studies (Annesley and Madore, 1994; Annesley et al., 1992, 1997a, b,
730 c; Annesley et al., 2005; Jeanneret et al., 2017; Martz, 2017). The end of this period is associated with pronounced
731 retrograde transformations, including the breakdown of cordierite to phyllosilicates, biotite chloritization, sulfide,
732 graphite and muscovite precipitation, quartz-rich fluid circulation, and dissolution-reprecipitation of monazite and
733 zircon (Card, 2012, 2013; Card and Noll, 2016). These processes are further constrained by cooling ages obtained
734 from Rb-Sr biotite (Worden et al., 1985; Schneider et al., 2007), K-Ar muscovite (Philippe et al., 1993), and Ar-
735 Ar muscovite (Alexandre et al., 2009). This timeframe has also been interpreted as reflecting a late thermal event
736 associated with the emplacement of the Kivalliq Igneous Suite (KIS) to the northeast of the Athabasca Basin, with
737 the Wollaston Domain being intruded by the Nueltin Granite of the same suite (ca. 1770-1730 Ma), which may
738 have reset U-Pb metamorphic rutile ages (Adlakha and Hattori, 2021). Additionally, hydrothermal graphite,
739 commonly spatially associated with early hydrothermal muscovite within the Wollaston-Mudjatik Transition shear
740 zones, yields highly precise (<1 %) Re-Os isochron ages of 1731.5 ± 7.4 Ma (2σ ; MSWD = 1.3). These ages are
741 interpreted to record graphite formation during the exhumation and orogenic cooling phase of the THO (Martz,
742 2017) and/or a period of elevated heat flow associated with the KIS emplacement (Adlakha and Hattori, 2021),
743 wherein aqueous fluids mobilized carbon from adjacent wall rocks into semi-brittle to brittle-ductile shear zones
744 (Toma et al., 2022). Overall, the Rb-Sr single-spot ages of early hydrothermal muscovite are consistent with the
745 exhumation and orogenic cooling stage of the THO, during which anatetic granitoids were emplaced and/or
746 magmatic activity of the Kivalliq Igneous Suite occurred, and they further align with the circulation of carbon-
747 bearing aqueous fluids responsible for the formation of hydrothermal graphite. Comparison of the Rb-Sr ages
748 obtained from alteration-free metamorphic and early hydrothermal muscovite with existing literature datasets
749 indicates that the Rb-Sr system constitutes a suitable geochronometer in this geological context, as evidenced by
750 the reproducibility of comparable Rb-Sr ages across four distinct sites within the WMTZ of the THO (Fig. 10).

751 **5.3. Assessing the reliability and applicability of the Rb-Sr system to date hydrothermal system in
752 crystalline basement**

753 Variably altered muscovite crystals occurring in illite-sudoite hydrothermal alteration zones in the four study sites
754 along the WMTZ in the eastern Athabasca Basin display highly scattered Rb-Sr single-spot dates and substantial
755 individual uncertainties, ranging from 1756.2 ± 22.9 to 1504.9 ± 11.1 Ma. Despite this variability, muscovite from
756 both altered pelitic and granitic protoliths shows comparable Rb-Sr single spot data distributions. Gaussian
757 Mixture Modelling (GMM) and radial plot analysis define five statistically coherent populations shared by both
758 muscovite generations affected by illite-sudoite alteration. However, their geochronological resolution is
759 intrinsically limited because the analytical uncertainties are large. This reflects the inherent difficulty of precisely
760 dating Paleoproterozoic geological events, as all isotopic systems tend to yield significant errors at such ancient
761 ages (e.g., Fayek et al., 2002b; Alexandre et al., 2005; Rainbird et al., 2007; Schneider et al., 2007; Davis et al.,
762 2011; Jeanneret et al., 2017; Adlakha and Hattori, 2021; Toma et al., 2022). The identification of five sub-
763 populations does not imply that this is the only possible partitioning, but rather the one favored by the model under
764 the present configuration, given the single-spot age values and their associated uncertainties. Small sub-
765 populations should likewise be interpreted cautiously: although they may correspond to genuine age modes, they
766 may also reflect asymmetries, outliers, or an artificial segmentation of an otherwise continuous distribution.
767 Several studies have demonstrated that Gaussian mixture models can generate artificial components when fitting



768 continuous or asymmetric distributions (McLachlan & Peel, 2000; Bishop, 2006; Hastie et al., 2009). When
769 substantial overlap exists between Gaussian components, the model often represents a single underlying population
770 using multiple components (Fraley & Raftery, 2002). Ultimately, the components should be regarded primarily as
771 probabilistic centers, which we attempt to compare with published datasets from the literature (Figs. 8, 10).

772 A dominant population at ca. 1640 Ma, representing the majority of the dataset and potentially overlooked without
773 prior petrographic constraints, is consistently recorded across four independent sites within the WMTZ of the
774 THO, supporting the regional significance and robustness of this age population. This main cluster is accompanied
775 by subordinate age groups at ca. 1680 Ma, ca. 1600 Ma, ca. 1550 Ma, and by a minor population near ca. 1467
776 Ma, which display limited inter-site variability and likely reflect local heterogeneities or superimposed geological
777 processes. These ages fall within the post-Athabasca Basin evolution, following basin deposition between ca. 1760
778 and 1720 Ma (Ramaekers et al., 2007; Jeanneret et al., 2016) and continuing until ca. 1541 Ma (Creaser and
779 Stasiuk, 2007). The data obtained in strongly illite-sudoite-altered zones of the basement, spatially associated with
780 the uranium mineralization, record extensive mineralogical transformations and major geochemical and isotopic
781 modifications driven by the circulation of basinal brines; i.e., the same fluids responsible for the characteristic
782 illite-sudoite alteration halos observed around all unconformity-related uranium deposits in the eastern Athabasca
783 Basin. The spread of the Rb-Sr single-spot dates may reflect either a single, long-lived fluid-rock interaction event
784 with a paroxysm at ca. 1640 Ma, or a sequence of pulsed hydrothermal episodes represented by the GMM and
785 radial plot populations.

786 The main peak at ca. 1640 Ma is widely recognized across the basin as marking a major sedimentary reorganization
787 event associated with a rapid westward deepening and the deposition of deeper-water successions (ca. 1664-1590
788 Ma; e.g., Pehrsson et al., 2023). This structural tilting correlates with the Racklan-Forward orogeny (ca. 1660-
789 1590 Ma; e.g., Furlanetto et al., 2016; Pehrsson et al., 2023), a far-field intracontinental compressional event that
790 reactivated deep crustal faults and deformed the northern Laurentian basement. Within the same time interval,
791 zircon extracted from reworked tuff intraclasts of the Wolverine Point Formation (member b) yields a weighted
792 mean $^{207}\text{Pb}/^{206}\text{Pb}$ age of 1644 ± 13 Ma (2σ), interpreted as the crystallization age of the original tuff layers
793 (Rainbird et al., 2007; Fig. 10). These tuffs are considered to be correlative with the Yavapai and Mazatzal
794 Paleoproterozoic orogens, particularly within the Cochise block of the Mazatzal orogen, where juvenile arc
795 terranes and syntectonic plutons range from ca. 1660 to 1600 Ma (Sims and Peterman, 1986; Karlstrom and
796 Bowring, 1988; Eisele and Isachsen, 2001; Rainbird et al., 2007). In a broader geodynamic framework, this event
797 may also be linked to the Racklan Orogeny of northwestern Laurentia, interpreted as the northwestern continuation
798 of the Mazatzal orogenic system. Together, these orogenic events define a large-scale Paleoproterozoic
799 accretionary system that affected the margins of the Canadian Shield and promoted significant crustal reworking,
800 consistent with the hypothesis of a circum-Laurentian orogenic belt (e.g., Furlanetto et al., 2013). U-Pb data
801 obtained from fluorapatite in the Athabasca Basin indicate a coherent phase of phosphate cementation, constrained
802 by weighted mean $^{207}\text{Pb}/^{206}\text{Pb}$ ages obtained on apatite with high radiogenic-to-common Pb ratios, and by Pb-Pb
803 regression lines that are independent of common Pb (e.g., Davis et al., 2011). Fluorapatite from the Smart, Manitou
804 Falls, and Wolverine Point formations of the Athabasca Basin yielded ages of 1609 ± 30 Ma, 1638 ± 12 Ma, and
805 1625 ± 17 Ma, respectively, clustering around a mean age of approximately 1630 ± 9 Ma (e.g., Davis et al., 2011;
806 Fig. 10). These ages are interpreted to record a basin-wide circulation of warm, oxidizing, P-rich brines produced
807 by fluid-rock interactions between basinal brines and the altered crystalline basement during mesogenetic



808 diagenesis. This large-scale fluid circulation is likely tectonically driven and related to the regional geodynamic
809 evolution of the basin, as proposed by Pehrsson et al. (2023), and can be temporally constrained to ca. 1640 Ma
810 based on the concordance between Rb-Sr and U-Pb apatite ages. Illite-sudoite alteration dated at ca. 1640 Ma can
811 be interpreted in two alternative, but not mutually exclusive, ways. First, this alteration may predate the main stage
812 of uranium oxide precipitation, commonly dated between ca. 1590 and 1200 Ma based on U-Pb analyses of
813 uraninite and K-Ar/Ar-Ar geochronology of clay minerals (Cumming and Krstic, 1992; Philippe et al., 1993;
814 McGill et al., 1993; Fayek et al., 2002b; Alexandre et al., 2009; Cloutier et al., 2011; Powell et al., 2022). In this
815 scenario, the ca. 1640 Ma illite-sudoite alteration would represent a basin-scale hydrothermal event that prepared
816 the basement-basin interface for subsequent uranium mineralization by enhancing permeability, redox reactivity,
817 and uranium mobility. Alternatively, the 1640 Ma alteration may record an early phase of uranium mineralization
818 itself, subsequently overprinted and partially reset by younger tectono-hydrothermal events. Such a model is
819 consistent with studies demonstrating that the U-Pb systematics of uraninite and associated alteration minerals in
820 unconformity-related uranium deposits are commonly affected by multiple fluid-flow episodes, leading to partial
821 Pb loss and a wide dispersion of apparent ages (Kotzer and Kyser, 1990; Fayek and Kyser, 1997; Fayek et al.,
822 2002a,b; Kyser et al., 2015). Consequently, an older hydrothermal and/or mineralizing system active during the
823 ca. 1680-1640 Ma interval cannot be excluded, but may remain cryptic due to subsequent uranium remobilization
824 and isotopic resetting during younger basin-wide fluid circulation events. This interpretation is further supported
825 by analogues from northern Australia, where *in situ* U-Pb analyses of uraninite indicate initial mineralization or
826 hydrothermal alteration as early as ca. 1680-1640 Ma, followed by multiple resetting episodes extending into the
827 Mesoproterozoic and Paleozoic (Clauer et al., 2015; Skirrow et al., 2016).

828 In addition to the main population associated with illite-sudoite alteration at ca. 1640 Ma, several consistent
829 statistical sub-populations are identified by the GMM. However, no chemical or mineralogical modifications are
830 observed in the zones where these single-spot data were measured. A first sub-population calculated around ca.
831 1680 Ma can be interpreted in two ways. It may represent a mixed population between preserved and altered data
832 (Fig. 6F), reflecting the onset of alteration and a partial loss of radiogenic ^{87}Sr caused by this early alteration stage
833 at ca. 1640 Ma. Such mixing would tend to skew the single-spot Rb-Sr dates of metamorphic muscovite, which
834 crystallized prior to early hydrothermal muscovite, toward older dates. Alternatively, this ca. 1680 Ma population
835 could correspond to an argillization episode dated to this period by Alexandre et al. (2009) using Ar-Ar analyses
836 on basement-hosted illite, which yielded pseudo-plateau ages at McArthur River of 1669 ± 4 Ma, 1666 ± 6 Ma,
837 and 1671 ± 7 Ma, interpreted as a pre-ore alteration event (Fig. 10). However, the actual geological significance
838 of each published age and its attribution to a specific event are often difficult to evaluate in this context, due to
839 successive episodes of intense fluid circulation and associated fluid-rock interaction processes that promote
840 substantial Ar loss and consequently yield younger ages (Chi et al., 2018). Nevertheless, during this time interval,
841 the basin is characterized by a half-graben architecture, with sediment transport predominantly directed toward the
842 northwest and enhanced sediment accumulation along the southeastern basin margin. This configuration reflects
843 an intracontinental extensional regime established after the THO orogeny, which may have facilitated the
844 circulation of early fluids within the basement and may also have reset the Rb-Sr system.

845 The sub-populations at ca. 1600 Ma and ca. 1550 Ma document hydrothermal activity previously identified in the
846 Athabasca Basin and its underlying basement, although it remains unclear whether they reflect a single event, a
847 series of pulsatile episodes, or processes potentially related to, or distinct from, the ca. 1640 Ma event. This



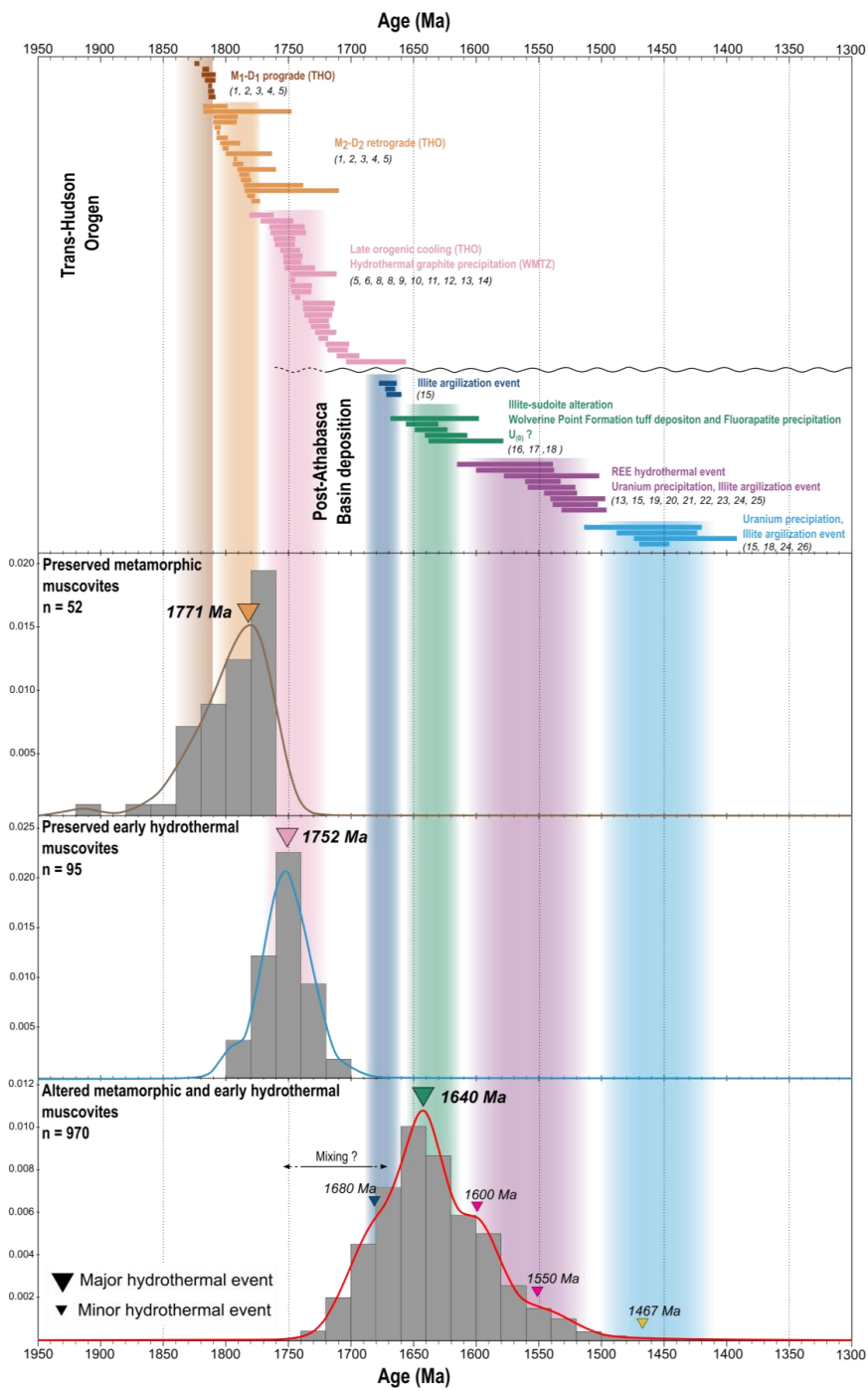
848 hydrothermal activity is highlighted in the basement by anatase precipitation, a low-pressure, low-temperature
849 TiO_2 polymorph, yielding a weighted mean $^{207}\text{Pb}/^{206}\text{Pb}$ age of 1569 ± 31 Ma (MSWD = 0.30, n = 5, 2σ ; Adlakha
850 and Hattori, 2021, Fig. 10). This age has been interpreted as reflecting the onset of oxidizing hydrothermal activity
851 in the basement, contemporaneous with U precipitation at the world-class McArthur River deposit, which has been
852 dated by U-Pb analyses of U oxides with two discordant ages of 1540 ± 19 Ma (Alexandre et al., 2009) and 1540
853 ± 38 Ma (Alexandre and Kyser, 2005). Additional ages at ca. 1520 Ma, including 1514 ± 18 Ma (Cummings and
854 Krstic, 1992), 1519 ± 22 Ma (Fayek et al., 2002b), and 1521 ± 18 Ma (McGill et al., 1993), have been interpreted
855 as minimum crystallization ages for primary uraninite. An episode of argillization contemporaneous with these
856 fluid-circulation events has also been identified at 1577 ± 38 Ma (K-Ar muscovite from gneiss; Philippe et al.,
857 1993) at Cigar Lake, and at 1533 ± 13 Ma (Ar-Ar on illite; Alexandre et al., 2009) at McArthur River. A further
858 rare-earth-phosphate hydrothermal episode is documented in the eastern Athabasca Basin within the Maw Zone
859 rare-earth-element deposit. U-Pb dating of xenotime yielded a $^{207}\text{Pb}/^{206}\text{Pb}$ age of 1547 ± 14 Ma (Rabiee et al., 2017;
860 Fig. 10), and both isotopic signatures and fluid-inclusion characteristics support the interpretation that the fluids
861 responsible for xenotime precipitation were part of the same oxidizing-reducing hydrothermal system involved in
862 the development of major uraninite mineralization across the Athabasca Basin. More broadly, these events are
863 associated with a renewed phase of subsidence and marine flooding, attributed to intracontinental rifting or
864 extension and linked to the emplacement of the Kuungmi Formation basalts in the adjacent Thelon Basin. This
865 rifting episode coincides with a reorganization of the Laurentian crust following the Australia-Laurentia collision,
866 and precedes the stabilization of Nuna, potentially promoting large-scale fluid circulation through both the
867 basement and the basin, capable of resetting the Rb-Sr geochronometer in muscovite.

868 Finally, the minor population at ca. 1467 Ma could correspond to a first mineralizing event recorded in the Cigar
869 Lake deposit by discordant U-Pb ages of 1467 ± 47 Ma (Fayek et al., 2002b) and weighted mean $^{207}\text{Pb}/^{206}\text{Pb}$ ages
870 of 1458 ± 12 Ma (Kister, 2003). An argillization event contemporaneous with these fluid-circulation episodes has
871 also been identified at 1456 ± 32 Ma (K-Ar on the $<2 \mu\text{m}$ fraction from gneiss; Philippe et al., 1993) at Cigar Lake,
872 and at 1433 ± 31 Ma (Ar-Ar on illite; Alexandre et al., 2009) at McArthur River. Overall, current data do not allow
873 discrimination between a single protracted fluid-rock interaction episode at ca. 1640 Ma leading to the formation
874 of an illite-sudoite alteration halo and multiple episodic fluid pulses to account for the Rb-Sr single-spot age
875 distribution in altered metamorphic and early hydrothermal muscovite. Nevertheless, these results clearly
876 demonstrate the applicability of the Rb-Sr chronometer for constraining hydrothermal fluid circulation at basin-
877 basement interfaces. The distinct age populations identified in muscovite and alteration products correspond to
878 tectono-hydrothermal events that are independently recognized in the regional geological record and have been
879 previously dated using other geochronological methods. Comparable multi-stage fluid-thermal histories have been
880 documented in other hydrothermal systems, such as gold deposit systems, where primary mineral phases
881 commonly preserve evidence for repeated isotopic resetting, trace-element redistribution, and microstructural
882 overprinting associated with episodic fluid and heat input (e.g., Bevan et al., 2021; Chen et al., 2024; Drake et al.,
883 2023; Huang et al., 2023; Liu et al., 2018; Mao et al., 2013; Olierook et al., 2020; Redaa et al., 2021, 2022; Şengün
884 et al., 2019; Wang et al., 2022; Zametzer et al., 2022; Tian et al., 2024; Boschetti et al., 2025; Huang et al., 2025).
885 Such behaviour underscores the capacity of mineral-scale chronometers to resolve protracted hydrothermal
886 evolution. In this context, the present data suggest that the Rb-Sr system in muscovite and alteration minerals is
887 sensitive to successive hydrothermal events at basin-basement interfaces, highlighting its potential as a robust tool



888 for reconstructing the timing and duration of fluid circulation processes, while emphasizing the need for further
889 work to evaluate mineralogical and geochemical controls on system behaviour. Although these initial results are
890 promising, further work is required to assess potential mineralogical or geochemical specificities that may
891 influence the Rb-Sr system under such conditions.

892



893

894 Figure 10. Compilation of published geochronological constraints for the Trans-Hudson orogen and the Athabasca Basin, integrated
 895 with the new Rb-Sr single-spot ages obtained in this study. The onset of sedimentation in the Athabasca Basin occurred at ca. 1760-



896 1720 Ma (Ramaekers et al., 2007; Jeanneret et al., 2016). The diagram synthesizes available ages documenting the prograde
897 metamorphic path, the retrograde evolution, and the late-orogenic cooling stages of the Trans-Hudson orogen, together with the timing
898 of hydrothermal events recorded both in the Athabasca Basin and in its crystalline basement. Literature ages are derived from multiple
899 minerals and chronometers. Included datasets comprise: U-Pb on zircon and monazite from (1) Annesley et al., 1992; (2) Annesley et
900 al., 1997; (3) Annesley et al., 1999; (4) Toma et al., 2024; (5) Jeanneret et al., 2016; (6) Card, 2012; (7) Card, 2014; (8) Card and Noll,
901 2016; Rb-Sr on biotite from (9) Worden et al., 1985; (10) Schenier et al., 2007; U-Pb on rutile from (11) Adlakha and Hattori, 2021;
902 Ar-Ar on muscovite from (12) Alexandre et al., 2009; K-Ar on muscovite from (13) Philippe et al., 1993; Re-Os on graphite from (14)
903 Toma et al., 2024); Ar-Ar on illite from (15) Alexandre et al., 2009; U-Pb on zircon from (16) Rainbird et al., 2017); U-Pb on fluorapatite
904 from (17) Davis et al., 2011); K-Ar on <2 µm fractions from gneiss from (18) Philippe et al., 1993; U-Pb on xenotime from (19) Rabiei
905 et al., 2017); U-Pb on anatase from (20) Adlakha and Hattori, 2021); U-Pb on UO₂ from (21) Alexandre et al., 2009; (22) Alexandre and
906 Kyser, 2005; (23) Cummings and Krstic, 1992; (24) Fayeck et al., 2002b; (25) McGill et al., 1993; (26) Kister, 2003). Probability density
907 distribution and histogram plots of Rb-Sr single-spot ages obtained from preserved early hydrothermal and metamorphic muscovite
908 unaffected by post-crystallization alteration are correlated with recognized Trans-Hudson orogenic events. Probability density
909 distribution and histogram plots of Rb-Sr single-spot ages derived from muscovites overprinted by post-crystallization illite-sudoite
910 alteration are presented along with the results of a Gaussian Mixture Model (GMM) used to identify distinct age components. The
911 central age population at ca. 1640 Ma is interpreted to record the main illite-sudoite hydrothermal alteration event, whereas
912 subordinate components may correspond to additional hydrothermal pulses documented in the literature.

913 6. Conclusions

914 This study tests the relevance and limitations of the Rb-Sr chronometer applied to muscovite from pelitic gneisses,
915 including migmatites, and granitoids from the Paleoproterozoic basement of the Wollaston-Mudjatik Transition
916 Zone, within the context of hydrothermal alteration (formed by an association of illite and sudoite) associated with
917 the formation of Athabasca Basin unconformity-related uranium deposits. The primary objective was to determine
918 to what extent this isotopic system, conventionally used to date the crystallization or cooling of crustal rocks, can
919 also record and quantify late-stage fluid circulation events, despite the complexity induced by partial system
920 reopening through fluid-rock interaction.

921 Petrographic and isotopic analyses of preserved domains demonstrate that, in areas lacking illite-sudoite alteration,
922 metamorphic and early hydrothermal muscovite yield ages of ca. 1780 Ma and ca. 1750 Ma, respectively. Retro-
923 metamorphic muscovite specifically records the transition to temperatures below its closure temperature (450-600
924 °C), marking cooling, possibly in the presence of fluids, following the peak metamorphism and isothermal
925 decompression of the THO basement. Early hydrothermal muscovite, in turn, records the exhumation and orogenic
926 cooling phase of the THO, during which anatexic granitoids were emplaced and/or magmatic activity of the
927 Kivalliq Igneous Suite occurred. Its formation is also consistent with the circulation of carbon-bearing aqueous
928 fluids that facilitated the development of hydrothermal graphite. These results demonstrate that, in minimally
929 altered domains, the Rb-Sr system yields ages consistent with established geochronological constraints obtained
930 from independent isotopic systems and mineral phases for both episodes, thereby confirming that the Rb-Sr
931 chronometer remains fully reliable for dating the terminal Paleoproterozoic thermo-metamorphic events.

932 In contrast, muscovite from pelitic gneiss or granitic protoliths affected by illite-sudoite alteration developed after
933 the deposition of the Athabasca Basin displays deeply modified mineralogical, geochemical, and isotopic
934 signatures. These signatures reflect the micrometre-scale reopening of the Rb-Sr isotopic system through fluid-
935 rock interaction during brine circulation, in response to the structural destabilization of muscovite during
936 illitization and/or sudoitization. The preferential transfer of radiogenic ⁸⁷Sr into clay phases and/or the fluid phase
937 constitutes the major mechanism driving isotopic resetting.



938 The dominant population of Rb-Sr single spot data at ca. 1640 Ma reflects a major hydrothermal event. This age
939 interval coincides with a first-order sedimentary reorganization of the basin and with crustal-scale reactivation
940 related to the late Paleoproterozoic Racklan-Mazatzal orogenic system (ca. 1.66-1.59 Ga), which affected the
941 northwestern to southern margins of Laurentia and the adjacent edge of the Canadian Shield. These tectonic
942 processes are accompanied by widespread fluid circulation and diagenetic to hydrothermal events in the Athabasca
943 Basin, as independently documented by U-Pb ages obtained on fluorapatite. Comparison with other
944 geochronological constraints and regional geodynamic reconstructions supports the interpretation that the ages
945 measured on altered muscovite and associated alteration products are geologically meaningful and temporally
946 consistent. Rather than reflecting localized or spurious resetting, these ages are best interpreted as recording a
947 geologically realistic and regionally significant hydrothermal event, broadly coeval with the Racklan-Mazatzal
948 orogenic continuum, which represents the northwestern expression of a circum-Laurentian orogenic belt affecting
949 the margins of the Canadian Shield. It corresponds to the principal illite-sudoite alteration event responsible for
950 the mineralized halos around uranium deposits and represents the key event recorded by altered muscovites.
951 Additional age populations reflect further hydrothermal episodes or fluid-reactivation phases: (i) ca. 1680 Ma,
952 possibly linked to a pre-ore argillization event documented by Ar-Ar ages on illite, or to an initial stage of partial
953 disturbance of the Rb-Sr system; (ii) ca. 1600 Ma and ca. 1550 Ma, corresponding to a major oxidizing
954 hydrothermal phase concomitant with a mineralizing event, recognized from U-Pb ages on anatase, xenotime, and
955 uraninite, notably at McArthur River; (iii) ca. 1467 Ma, associated with a major mineralizing episode recorded in
956 the district (Cigar Lake).

957 This study demonstrates that the *in situ* Rb-Sr geochronometer applied to muscovite and related alteration products
958 constitutes a relevant tool not only for constraining late-metamorphic and late-magmatic and/or early hydrothermal
959 histories in unaltered domains, but also for identifying and dating post-crystallization hydrothermal circulation
960 events after basin sedimentation, associated with unconformity-related metallic deposits. By coupling detailed
961 petrographic analysis with *in situ* geochemical characterization, it becomes possible to distinguish preserved ages
962 reflecting Paleoproterozoic crystallization or cooling from reset ages marking Mesoproterozoic hydrothermal
963 episodes. The Rb-Sr chronometer thus emerges as a powerful and complementary tool within the existing suite of
964 fluid tracers, opening new perspectives for the temporal and spatial reconstruction of paleo-hydrothermal systems
965 across basin-basement interfaces.

966 **Code and data availability**

967 All data supporting the findings of this study are provided in the Appendix.

968 **Supplement**

969 The supplement related to this article is available at:

970 **Author contributions**

971 Conceptualization: QB, JM; Fieldwork: QB, GM, EF, TO, AK, JM; Methodology and data acquisition: QB, CP,
972 AL, JM; Data curation: QB, MS, TO, CP, AL, JM; Writing (original draft preparation): QB, GM, EF, CB, AL, PM,
973 JM; Funding acquisition: JM.

974 **Competing interests**



975 The authors declare that they have no conflict of interest.

976 **Disclaimer**

977 Publisher's note: Copernicus Publications remains neutral with regard to jurisdictional claims made in the text,
978 published maps, institutional affiliations, or any other geographical representation in this paper. While Copernicus
979 Publications makes every effort to include appropriate place names, the final responsibility lies with the authors.

980 **Acknowledgements**

981 The French Agence Nationale de la Recherche (ANR) and Orano are thanked for funding this project. The authors
982 gratefully acknowledge Orano Canada and Cameco for providing access to the field sites, samples, and data
983 transfer. Special thanks are extended to Charles Khairallah, Magdalena Anderson, Andrew Kaczowka, and Gerard
984 Zaluski for their valuable assistance during the field missions and data sharing.

985 **Financial support**

986 This research has been supported by the French Agence Nationale de la Recherche (ANR) and Orano, under grant
987 ANR-21-CHIN-0006 (project GeomIn3D).

988 **References**

989 Adlakha, E. E., and Hattori, K.: Compositional variation and timing of aluminum phosphate-sulfate minerals in
990 the basement rocks along the P2 fault and in association with the McArthur River uranium deposit, Athabasca
991 Basin, Saskatchewan, Canada, *Am. Mineral.*, 100, 1386-1399, 10.2138/am-2015-5069, 2015.

992 Adlakha, E., and Hattori, K.: Thermotectonic events recorded by U-Pb geochronology and Zr-in-rutile
993 thermometry of Ti oxides in basement rocks along the P2 fault, eastern Athabasca Basin, Saskatchewan, Canada,
994 *Geol. Soc. Am. Bull.*, 134, 567-576, 10.1130/B35820.1, 2021.

995 Aldega, L., Viola, G., Casas-Sainz, A., Marcén, M., Román-Berdiel, T., and van der Lelij, R.: Unraveling Multiple
996 Thermotectonic Events Accommodated by Crustal-Scale Faults in Northern Iberia, Spain: Insights From K-Ar
997 Dating of Clay Gouges, *Tectonics*, 38, 3629-3651, <https://doi.org/10.1029/2019TC005585>, 2019.

998 Alexandre, P., Kyser, K., Polito, P., and Thomas, D.: Alteration mineralogy and stable isotope geochemistry of
999 Paleoproterozoic basement-hosted unconformity-type uranium deposits in the Athabasca Basin, Canada, *Econ.*
1000 *Geol.*, 100, 1547-1563, 10.2113/gsecongeo.100.8.15473, 2005.

1001 Alexandre, P. and Kyser, T. K.: GEOCHEMISTRY OF URANIFEROUS BITUMEN IN THE SOUTHWEST
1002 ATHABASCA BASIN, SASKATCHEWAN, CANADA, *Economic Geology*, 101, 1605-1612,
1003 <https://doi.org/10.2113/gsecongeo.101.8.1605>, 2006.

1004 Alexandre, P., Kyser, K., Thomas, D., Polito, P., and Marlat, J.: Geochronology of unconformity-related uranium
1005 deposits in the Athabasca Basin, Saskatchewan, Canada and their integration in the evolution of the basin, *Miner.*
1006 *Deposita*, 44, 41-59, 10.1007/s00126-007-0153-3, 2009.



1007 Alexandre, P., Jiricka, D., and Witt, G.: Formation and evolution of the Centennial unconformity-related uranium
1008 deposit in the south-central Athabasca Basin, Canada, *Econ. Geol.*, 107, 385-400, 10.2113/econgeo.107.3.385,
1009 2012.

1010 Anders, M. H., Laubach, S. E., and Scholz, C. H.: Microfractures: A review, *Journal of Structural Geology*, 69,
1011 377-394, <https://doi.org/10.1016/j.jsg.2014.05.011>, 2014.

1012 Ansdel, K. M.: Tectonic evolution of the Manitoba-Saskatchewan segment of the Paleoproterozoic Trans-Hudson
1013 Orogen, Canada, *Can. J. Earth Sci.*, 42, 741-759, <https://doi.org/10.1139/e05-035>, 2005.

1014 Annesley, I., Madore, C., and Krogh, T. E.: U-Pb geochronology of some granitoids from the Peter Lake Domain:
1015 A summary, *Summary of Investigations, Saskatchewan Geological Survey, Saskatchewan Energy and mines,*
1016 *Miscellaneous Report*, 168-171, 1992.

1017 Annesley, I.R., and Madore, C.: A geological study of the Wollaston-Mudjatik domain boundary in the Wollaston
1018 Lake area, Hearne Province, Saskatchewan, *Saskatchewan Research Council, Publ. R-1230-6-C-94*, 162 p., 1994.

1019 Annesley, I.R., Madore, C., and Shi, R.: Thermotectonic evolution of the Wollaston EAGLE Project Area ,
1020 *Saskatchewan Research Council, Publ. R-1420-2-C-97, Part 1*, 1-62, 1997a.

1021 Annesley, I., Madore, C., Shi, R., and Krogh, T.: U-Pb geochronology of thermotectonic events in the Wollaston
1022 Lake area, Wollaston Domain: A summary of 1994-1996 results, *Summary of Investigations 1997, Saskatchewan*
1023 *Geological Survey, Saskatchewan Energy and Mines*, 1, 162-173, 1997b.

1024 Annesley, I.R., Madore, C., and Krogh, T.E.: U-Pb geochronology of peraluminous pegmatites from the Wollaston
1025 Lake area, northern Saskatchewan, *Geol. Assoc. Can.-Mineral. Assoc. Can. Annual Meeting, Program with*
1026 *Abstracts*, 22, A-4, 1997c.

1027 Annesley, I.R., Madore, C., Shi, R., and Krogh, T.E: U-Pb geochronology and thermotectonic history of the
1028 Wollaston Domain in the Wollaston Lake area, Hearne Province, Saskatchewan, *Geol. Assoc. Can.-Mineral. Assoc.*
1029 *Can. Annual Meeting, Program with Abstracts*, 21, A-4, 1999a.

1030 Annesley, I.R., Madore, C., Krogh, T.E., Kwok, Y.Y., and Kamo, S.L.: New U-Pb zircon and
1031 monazite geochronological results for Archean and Paleoproterozoic basement to the southeastern part of the
1032 Athabasca Basin, *Saskatchewan Geological Survey, Misc. Rep. 99-4.2*, 90-99, 1999b.

1033 Annesley, I. R., Madore, C., and Portella, P.: Geology and thermotectonic evolution of the western margin of the
1034 Trans-Hudson Orogen: evidence from the eastern sub-Athabasca basement, *Saskatchewan, Can. J. Earth Sci.*, 42,
1035 573-597, <https://doi.org/10.1139/e05-034>, 2005.

1036 Beaufort, D., Patrier, P., Laverret, E., Bruneton, P., and Mondy, J.: Clay Alteration Associated with Proterozoic
1037 Unconformity-Type Uranium Deposits in the East Alligator Rivers Uranium Field, Northern Territory, Australia,
1038 *Economic Geology*, 100, 515-536, <https://doi.org/10.2113/gsecongeo.100.3.515>, 2005.

1039 Bevan, D., Coath, C. D., Lewis, J., Schwieters, J., Lloyd, N., Craig, G., Wehrs, H., and Elliott, T.: In situ Rb-Sr
1040 dating by collision cell, multicollection inductively-coupled plasma mass-spectrometry with pre-cell mass-filter,
1041 (CC-MC-ICPMS/MS), *J. Anal. At. Spectrom.*, 36, 917-931, <https://doi.org/10.1039/D1JA00006C>, 2021.



1042 Boiron, M.-C., Cathelineau, M., and Richard, A.: Fluid flows and metal deposition near basement /cover
1043 unconformity: lessons and analogies from Pb-Zn-F-Ba systems for the understanding of Proterozoic U deposits,
1044 *Geofluids*, 10, 270-292, <https://doi.org/10.1111/j.1468-8123.2010.00289.x>, 2010.

1045 Boschetti, L., Boulleterre, C., Rolland, Y., Schwartz, S., Milesi, G., Bienveignant, D., Macret, E., Charpentier, D.,
1046 Münch, P., Mercadier, J., Iemollo, A., Lanari, P., Rossi, M., and Moutherau, F.: Shear zone memory revealed by
1047 in-situ Rb-Sr and 40Ar/39Ar dating of Pyrenean and Alpine tectonic phases in the external Alps, *Lithos*, 514-515,
1048 108168, <https://doi.org/10.1016/j.lithos.2025.108168>, 2025.

1049 Bickford, M., Chiarenzelli, J., Van Schmus, W., Collerson, K. D., and Lewry, J.: Proterozoic collisional tectonism
1050 in the Trans-Hudson orogen, Saskatchewan, *Geology*, 18, 14-18, [https://doi.org/10.1130/0091-7613\(1990\)018-253C0014:PCTITT-253E2.3.CO;2](https://doi.org/10.1130/0091-7613(1990)018-253C0014:PCTITT-253E2.3.CO;2), 1990.

1052 Bickford, M. E., Mock, T. D., Steinhart Iii, W. E., Collerson, K. D., and Lewry, J. F.: Origin of the Archean Sask
1053 craton and its extent within the Trans-Hudson orogen: evidence from Pb and Nd isotopic compositions of basement
1054 rocks and post-orogenic intrusions, *Can. J. Earth Sci.*, 42, 659-684, <https://doi.org/10.1139/e04-064>, 2005.

1055 Bischoff, A., Heap, M. J., Mikkola, P., Kuva, J., Reuschlé, T., Jolis, E. M., Engström, J., Reijonen, H., and Leskelä,
1056 T.: Hydrothermally altered shear zones: A new reservoir play for the expansion of deep geothermal exploration in
1057 crystalline settings, *Geothermics*, 118, 102895, <https://doi.org/10.1016/j.geothermics.2023.102895>, 2024.

1058 Bishop, C. M. and Nasrabadi, N. M.: *Pattern recognition and machine learning*, Springer, 2006.

1059 Brigatti, M. F. and Guggenheim, S.: Mica Crystal Chemistry and the Influence of Pressure, Temperature, and Solid
1060 Solution on Atomistic Models, *Reviews in Mineralogy and Geochemistry*, 46, 1-97,
1061 <https://doi.org/10.2138/rmg.2002.46.01>, 2002.

1062 Brooks, C., Hart, S. R., Hofmann, A., and James, D. E.: Rb-Sr mantle isochrons from oceanic regions, *Earth and
1063 Planetary Science Letters*, 32, 51-61, [https://doi.org/10.1016/0012-821X\(76\)90184-9](https://doi.org/10.1016/0012-821X(76)90184-9), 1976.

1064 Bruneton, P.: Geological environment of the Cigar Lake uranium deposit, *Can. J. Earth Sci.*, 30, 653-673,
1065 <https://doi.org/10.1139/e93-054>, 1993.

1066 Campanha, G. A. C., Hueck, M., Wemmer, K., Esteves, M. C. B., Joncew, H. C., Faleiros, F. M., and Veloso, R. S.
1067 S.: Foreland deformation of Brasiliano orogens at the eastern and western margins of the São Francisco Craton:
1068 K-Ar illite dating of the Araçuá and Brasília fold-and-thrust belts, *JGS*, 183, [jgs2025-138](https://doi.org/10.1144/jgs2025-138),
1069 <https://doi.org/10.1144/jgs2025-138>, 2026.

1070 Card, C.: The Origins of Anomalously Graphitic Rocks and Quartzite Ridges in the Basement to the Southeastern
1071 Athabasca Basin, 2012.

1072 Card, C.: Altered Pelitic Gneisses and Associated " Quartzite Ridges " Beneath the Southeastern Athabasca Basin:
1073 Alteration Facies and their Relationship to Uranium Deposits along the Wollaston-Mudjatik Transition, 2014.

1074 Card, C. and Noll, J.: Host-Rock Protoliths, Pre-Ore Metasomatic Mineral Assemblages and Textures, and Exotic
1075 Rocks in the Western Athabasca Basin: Ore-System Controls and Implications for the Unconformity- Related
1076 Uranium Model, <https://doi.org/10.13140/RG.2.2.26473.70241>, 2016.



1077 Carl, C., Pechmann, E. V., Höhndorf, A., and Ruhrmann, G.: Mineralogy and U/Pb, Pb/Pb, and Sm/Nd
1078 geochronology of the Key Lake uranium deposit, Athabasca Basin, Saskatchewan, Canada, *Can. J. Earth Sci.*, 29,
1079 879-895, <https://doi.org/10.1139/e92-075>, 1992.

1080 Cathelineau, M., Boiron, M.-C., Fourcade, S., Ruffet, G., Clauer, N., Belcourt, O., Coulibaly, Y., Banks, D. A., and
1081 Guillocheau, F.: A major Late Jurassic fluid event at the basin/basement unconformity in western France:
1082 40Ar/39Ar and K-Ar dating, fluid chemistry, and related geodynamic context, *Chemical Geology*, 322-323, 99-
1083 120, <https://doi.org/10.1016/j.chemgeo.2012.06.008>, 2012.

1084 Chen, M., Chen, G., An, P., Zhang, L., and Wang, Y.: In situ illite Rb-Sr dating indicates the coevality of Carlin-
1085 type gold deposits inside and around the isolated carbonate platform in western Guangxi, China, *Ore Geology
1086 Reviews*, 165, 105905, <https://doi.org/10.1016/j.oregeorev.2024.105905>, 2024.

1087 Cherniak, D. J. and Watson, E. B.: Pb diffusion in zircon, *Chemical Geology*, 172, 5-24,
1088 [https://doi.org/10.1016/S0009-2541\(00\)00233-3](https://doi.org/10.1016/S0009-2541(00)00233-3), 2001.

1089 Cherniak, D. J., Watson, E. B., Grove, M., and Harrison, T. M.: Pb diffusion in monazite: a combined RBS/SIMS
1090 study, *Geochimica et Cosmochimica Acta*, 68, 829-840, <https://doi.org/10.1016/j.gca.2003.07.012>, 2004.

1091 Chi, G., Li, Z., Chu, H., Bethune, K. M., Quirt, D. H., Ledru, P., Normand, C., Card, C., Bosman, S., Davis, W. J.,
1092 and Potter, E. G.: A SHALLOW-BURIAL MINERALIZATION MODEL FOR THE UNCONFORMITY-
1093 RELATED URANIUM DEPOSITS IN THE ATHABASCA BASIN, *Economic Geology*, 113, 1209-1217,
1094 <https://doi.org/10.5382/econgeo.2018.4588>, 2018.

1095 Chiarenzelli, J.: Petrogenesis and tectonic significance of the Guncoat and Nistowiak gneisses, Glennie Lake
1096 Domain, northern Saskatchewan, Unpublished Ph. D. thesis, University of Kansas, 229, 1989.

1097 Chiarenzelli, J., Aspler, L., Villeneuve, M., and Lewry, J.: Early Proterozoic Evolution of the Saskatchewan Craton
1098 and Its Allochthonous Cover, Trans-Hudson Orogen, *The Journal of Geology*, 106, 247-268,
1099 <https://doi.org/10.1086/516020>, 1998.

1100 Clauer, N., Vidal, P., and Auvray, B.: Differential behaviour of the Rb-Sr and K-Ar systems of spilitic flows and
1101 interbedded metasediments: the spilite group of Erquy (Brittany, France). Paleomagnetic implications, *Contr.
1102 Mineral. and Petrol.*, 89, 81-89, <https://doi.org/10.1007/BF01177593>, 1985.

1103 Clauer, N., Šrodon, J., Francu, J., and Šucha, V.: K-Ar dating of illite fundamental particles separated from illite-
1104 smectite, *Clay Minerals*, 32, 181-196, <https://doi.org/10.1180/claymin.1997.032.2.02>, 1997.

1105 Clauer, N., Mercadier, J., Patrier, P., Laverret, E., and Bruneton, P.: Relating unconformity-type uranium
1106 mineralization of the Alligator Rivers Uranium Field (Northern Territory, Australia) to the regional Proterozoic
1107 tectono-thermal activity: An illite K-Ar dating approach, *Precambrian Research*, 269, 107-121,
1108 <https://doi.org/10.1016/j.precamres.2015.08.007>, 2015.

1109 Cloutier, J., Kyser, K., Olivo, G. R., Alexandre, P., and Halaburda, J.: The Millennium Uranium Deposit, Athabasca
1110 Basin, Saskatchewan, Canada: An Atypical Basement-Hosted Unconformity-Related Uranium Deposit, *Economic
1111 Geology*, 104, 815-840, <https://doi.org/10.2113/gsecongeo.104.6.815>, 2009.



1112 Cloutier, J., Kyser, K., Olivo, G. R., and Alexandre, P.: Contrasting Patterns of Alteration at the Wheeler River
1113 Area, Athabasca Basin, Saskatchewan, Canada: Insights into the Apparently Uranium-Barren Zone K Alteration
1114 System, *Economic Geology*, 105, 303-324, <https://doi.org/10.2113/gsecongeo.105.2.303>, 2010.

1115 Cloutier, J., Kyser, K., Olivo, G. R., and Brisbin, D.: Geochemical, isotopic, and geochronologic constraints on
1116 the formation of the Eagle Point basement-hosted uranium deposit, Athabasca Basin, Saskatchewan, Canada and
1117 recent remobilization of primary uraninite in secondary structures, *Miner Deposita*, 46, 35-56,
1118 <https://doi.org/10.1007/s00126-010-0308-5>, 2011.

1119 Corrigan, D.: Paleoproterozoic crustal evolution and tectonics processes: Insights from the LITHOPROBE
1120 program in the Trans-Hudson orogen, Canada, *Tectonic Styles in Canada: The LITHOPROBE Perspective*, 49,
1121 237-284, 2012.

1122 Corrigan, D., Hajnal, Z., Németh, B., and Lucas, S. B.: Tectonic framework of a Paleoproterozoic arc-continent to
1123 continent-continent collisional zone, Trans-Hudson Orogen, from geological and seismic reflection studies, *Can.*
1124 *J. Earth Sci.*, 42, 421-434, <https://doi.org/10.1139/e05-025>, 2005.

1125 Corrigan, D., Pehrsson, S., Wodicka, N., and De Kemp, E.: The Palaeoproterozoic Trans-Hudson Orogen: a
1126 prototype of modern accretionary processes, *SP*, 327, 457-479, <https://doi.org/10.1144/SP327.19>, 2009.

1127 Creaser, R. and Stasiuk, L. D.: Depositional age of the douglas formation, Northern Saskatchewan, determined by
1128 RE-Os geochronology, *Bulletin of the Geological Survey of Canada*, 341-346, 2007.

1129 Cumming, G. L. and Krstic, D.: The age of unconformity-related uranium mineralization in the Athabasca Basin,
1130 northern Saskatchewan, *Can. J. Earth Sci.*, 29, 1623-1639, <https://doi.org/10.1139/e92-128>, 1992.

1131 DePaolo, D. J.: Trace element and isotopic effects of combined wallrock assimilation and fractional crystallization,
1132 *Earth and Planetary Science Letters*, 53, 189-202, [https://doi.org/10.1016/0012-821X\(81\)90153-9](https://doi.org/10.1016/0012-821X(81)90153-9), 1981.

1133 Derome, D., Cathelineau, M., Cuney, M., Fabre, C., Lhomme, T., and Banks, D. A.: Mixing of Sodic and Calcic
1134 Brines and Uranium Deposition at McArthur River, Saskatchewan, Canada: A Raman and Laser-Induced
1135 Breakdown Spectroscopic Study of Fluid Inclusions, *Economic Geology*, 100, 1529-1545,
1136 <https://doi.org/10.2113/gsecongeo.100.8.1529>, 2005.

1137 Davis, W., Gall, Q., Jefferson, C. W., and Rainbird, R.: Fluorapatite in the Paleoproterozoic Thelon Basin:
1138 Structural-stratigraphic context, in situ ion microprobe U-Pb ages, and fluid-flow history, *Geological Society of*
1139 *America Bulletin*, 123, 1056-1073, <https://doi.org/10.1130/B30163.1>, 2011.

1140 Dickin, A. P.: Radiogenic Isotope Geology, 3rd ed., Cambridge University Press,
1141 <https://doi.org/10.1017/9781316163009>, 2018.

1142 Dodson, M. H.: Closure temperature in cooling geochronological and petrological systems, *Contr. Mineral. and*
1143 *Petrol.*, 40, 259-274, <https://doi.org/10.1007/BF00373790>, 1973.

1144 Drake, H., Tillberg, M., Reinhardt, M., Whitehouse, M. J., and Kooijman, E.: In Situ Rb/Sr Geochronology and
1145 Stable Isotope Geochemistry Evidence for Neoproterozoic and Paleozoic Fracture-Hosted Fluid Flow and



1146 Microbial Activity in Paleoproterozoic Basement, SW Sweden, *Geochem Geophys Geosyst*, 24, e2023GC010892,
1147 <https://doi.org/10.1029/2023GC010892>, 2023.

1148 Eberlei, T., Habler, G., Wegner, W., Schuster, R., Körner, W., Thöni, M., and Abart, R.: Rb/Sr isotopic and
1149 compositional retentivity of muscovite during deformation, *Lithos*, 227, 161-178,
1150 <https://doi.org/10.1016/j.lithos.2015.04.007>, 2015.

1151 Eisele, J. and Isachsen, C. E.: Crustal Growth in Southern Arizona: U-Pb Geochronologic and Sm-Nd Isotopic
1152 Evidence for Addition of the Paleoproterozoic Cochise Block to the Mazatzal Province, *American Journal of
1153 Science*, 301, 773-797, <https://doi.org/10.2475/ajs.301.9.773>, 2001.

1154 Etheridge, M. A., Wall, V. J., and Vernon, R. H.: The role of the fluid phase during regional metamorphism and
1155 deformation, *Journal Metamorphic Geology*, 1, 205-226, <https://doi.org/10.1111/j.1525-1314.1983.tb00272.x>,
1156 1983.

1157 Evans, J., MILLAR, I., and NOBLE, S.: Hydration during uplift is recorded by reset Rb-Sr whole-rock ages,
1158 *Journal of The Geological Society - J GEOL SOC*, 152, 209-212, <https://doi.org/10.1144/gsjgs.152.2.0209>, 1995.

1159 Faulkner, D. R., Jackson, C. A. L., Lunn, R. J., Schlische, R. W., Shipton, Z. K., Wibberley, C. A. J., and Withjack,
1160 M. O.: A review of recent developments concerning the structure, mechanics and fluid flow properties of fault
1161 zones, *Journal of Structural Geology*, 32, 1557-1575, <https://doi.org/10.1016/j.jsg.2010.06.009>, 2010.

1162 Faure, G., Mensing, T. M., and Faure, G.: Isotopes: principles and applications, Third edition., John Wiley & Sons,
1163 Inc, Hoboken, New Jersey, 897 pp., 2013.

1164 Fayek, M. and Kyser, T. K.: Characterization of multiple fluid-flow events and rare-earth-element mobility
1165 associated with formation of unconformity-type uranium deposits in the Athabasca Basin, Saskatchewan, *The
1166 Canadian Mineralogist*, 35, 627-658, 1997.

1167 Fayek, M., Harrison, T. M., Ewing, R. C., Grove, M., and Coath, C. D.: O and Pb isotopic analyses of uranium
1168 minerals by ion microprobe and U-Pb ages from the Cigar Lake deposit, *Chemical Geology*, 185, 205-225,
1169 [https://doi.org/10.1016/S0009-2541\(01\)00401-6](https://doi.org/10.1016/S0009-2541(01)00401-6), 2002a.

1170 Fayek, M., Kyser, T. K., and Riciputi, L. R.: U AND Pb ISOTOPE ANALYSIS OF URANIUM MINERALS BY
1171 ION MICROPROBE AND THE GEOCHRONOLOGY OF THE McARTHUR RIVER AND SUE ZONE
1172 URANIUM DEPOSITS, SASKATCHEWAN, CANADA, *The Canadian Mineralogist*, 40, 1553-1570,
1173 <https://doi.org/10.2113/gscanmin.40.6.1553>, 2002b.

1174 Fraley, C. and Raftery, A. E.: Model-Based Clustering, Discriminant Analysis, and Density Estimation, *Journal of
1175 the American Statistical Association*, 97, 611-631, <https://doi.org/10.1198/016214502760047131>, 2002.

1176 Frey, M., Bossennec, C., Seib, L., Bär, K., Schill, E., and Sass, I.: Interdisciplinary fracture network
1177 characterization in the crystalline basement: a case study from the Southern Odenwald, SW Germany, *Solid Earth*,
1178 13, 935-955, <https://doi.org/10.5194/se-13-935-2022>, 2022.

1179 Furlanetto, F., Thorkelson, D. J., Daniel Gibson, H., Marshall, D. D., Rainbird, R. H., Davis, W. J., Crowley, J. L.,
1180 and Vervoort, J. D.: Late Paleoproterozoic terrane accretion in northwestern Canada and the case for circum-



1181 1182 Columbian orogenesis, *Precambrian Research*, 224, 512-528, <https://doi.org/10.1016/j.precamres.2012.10.010>,
2013.

1183 1184 1185 1186 Furlanetto, F., Thorkelson, D. J., Rainbird, R. H., Davis, W. J., Gibson, H. D., and Marshall, D. D.: The Paleoproterozoic Wernecke Supergroup of Yukon, Canada: Relationships to orogeny in northwestern Laurentia and basins in North America, East Australia, and China, *Gondwana Research*, 39, 14-40, <https://doi.org/10.1016/j.gr.2016.06.007>, 2016.

1187 1188 Galbraith, R. F.: Graphical Display of Estimates Having Differing Standard Errors, *Technometrics*, 30, 271-281, <https://doi.org/10.2307/1270081>, 1988.

1189 1190 1191 Galbraith, R. F.: The radial plot: Graphical assessment of spread in ages, *International Journal of Radiation Applications and Instrumentation. Part D. Nuclear Tracks and Radiation Measurements*, 17, 207-214, [https://doi.org/10.1016/1359-0189\(90\)90036-W](https://doi.org/10.1016/1359-0189(90)90036-W), 1990.

1192 1193 1194 Gerardin, M., Milesi, G., Mercadier, J., Cathelineau, M., and Bartier, D.: Development of an integrated analytical platform for clay mineral separation, characterization and K-Ar dating, *Geoscientific Instrumentation, Methods and Data Systems*, 13, 309-323, <https://doi.org/10.5194/gi-13-309-2024>, 2024.

1195 1196 1197 Glodny, J. and Grauert*, B.: Evolution of a hydrothermal fluid-rock interaction system as recorded by Sr isotopes: A case study from the Schwarzwald, SW Germany, *Miner Petrol*, 95, 163-178, <https://doi.org/10.1007/s00710-008-0034-1>, 2009.

1198 1199 Glodek, M., Schels, M., and Schwenker, F.: Ensemble Gaussian mixture models for probability density estimation, *Comput Stat*, 28, 127-138, <https://doi.org/10.1007/s00180-012-0374-5>, 2013.

1200 1201 1202 1203 Grand'Homme, A., Janots, E., Bosse, V., Seydoux-Guillaume, A. M., and De Ascençao Guedes, R.: Interpretation of U-Th-Pb in-situ ages of hydrothermal monazite-(Ce) and xenotime-(Y): evidence from a large-scale regional study in clefts from the western alps, *Miner Petrol*, 110, 787-807, <https://doi.org/10.1007/s00710-016-0451-5>, 2016.

1204 1205 1206 Guillou-Frottier, L., Milesi, G., Roche, V., Duwiquet, H., and Taillefer, A.: Heat flow, thermal anomalies, tectonic regimes and high-temperature geothermal systems in fault zones, *Comptes Rendus. Géoscience*, 356, 389-421, <https://doi.org/10.5802/crgeos.213>, 2024.

1207 1208 1209 Gyomlai, T., Agard, P., Herviou, C., Jolivet, L., Monié, P., Mendes, K., and Lemmolo, A.: In situ Rb-Sr and 40Ar-39Ar dating of distinct mica generations in the exhumed subduction complex of the Western Alps, *Contrib Mineral Petrol*, 178, 58, <https://doi.org/10.1007/s00410-023-02042-8>, 2023.

1210 1211 1212 Halter, G.: Zonalite des alterations dans l'environnement des gisements d'uranium associes a la discordance du proterozoique moyen (saskatchewan, canada), *These de doctorat, Université Louis Pasteur (Strasbourg)* (1971-2008), 1988.

1213 1214 Hastie, T., Friedman, J., and Tibshirani, R.: *The Elements of Statistical Learning*, Springer New York, New York, NY, <https://doi.org/10.1007/978-0-387-21606-5>, 2001.



1215 Hobson, G. D., Canada, G. S. of, and MacAulay, H. A.: A Seismic Reconnaissance Survey of the Athabasca
1216 Formation, Alberta and Saskatchewan (part of 74), Department of Energy, Mines and Resources, 36 pp., 1969.

1217 Hoeve, J. and Sibbald, T. I. I.: On the genesis of Rabbit Lake and other unconformity-type uranium deposits in
1218 northern Saskatchewan, Canada, Economic Geology, 73, 1450-1473,
1219 <https://doi.org/10.2113/gsecongeo.73.8.1450>, 1978.

1220 Hogmalm, K. J., Zack, T., Karlsson, A. K.-O., Sjöqvist, A. S. L., and Garbe-Schönberg, D.: In situ Rb-Sr and K-
1221 Ca dating by LA-ICP-MS/MS: an evaluation of N₂O and SF₆ as reaction gases, J. Anal. At. Spectrom., 32, 305-
1222 313, <https://doi.org/10.1039/C6JA00362A>, 2017.

1223 Holness, M.: PARRELL, J. (ed.) 1998. Dating and Duration of Fluid Flow and Fluid-Rock Interaction. Geological
1224 Society Special Publication no. 144. vi+284 pp. Price £69.00, US \$115.00 (hard covers); members' price £35.00,
1225 US \$58.00. ISBN 1 86239 019 3. -, Geological Magazine, 137, 705-712,
1226 <https://doi.org/10.1017/S0016756800274736>, 2000.

1227 Huang, C., Wang, H., Xie, L., Xu, L., Wu, S., Yang, Y., and Yang, J.: High-precision Rb-Sr isotope analysis with
1228 Neoma MS/MS: Enhancing in situ geochronology by laser ablation, Spectrochimica Acta Part B: Atomic
1229 Spectroscopy, 224, 107117, <https://doi.org/10.1016/j.sab.2025.107117>, 2025.

1230 Huang, Y., Qi, X., Wu, Q., Li, J., Ren, M., Duan, L., Xiong, T., Yang, Z., Zhao, Y., Ciren, L., Wei, W., Duan, J.,
1231 and Yan, M.: In Situ Rb-Sr Dates of Muscovite and Sulfur Isotope of Pyrite from the Yangshan Gold Deposit in
1232 Western Qinling, China, Acta Geologica Sinica (Eng), 97, 1475-1489, <https://doi.org/10.1111/1755-6724.15091>,
1233 2023.

1234 Hueck, M., Wemmer, K., Ksienzyk, A. K., Kuehn, R., and Vogel, N.: Potential, premises, and pitfalls of interpreting
1235 illite argon dates - A case study from the German Variscides, Earth-Science Reviews, 232, 104133,
1236 <https://doi.org/10.1016/j.earscirev.2022.104133>, 2022.

1237 Jeanneret, P., Goncalves, P., Durand, C., Poujol, M., Trap, P., Marquer, D., Quirt, D., and Ledru, P.:
1238 Geochronological constraints on the trans-Hudsonian tectono-metamorphic evolution of the pre-Athabasca
1239 basement within the Wollaston-Mudjatik Transition Zone, Saskatchewan, Precambrian Research, 301, 152-178,
1240 <https://doi.org/10.1016/j.precamres.2017.07.019>, 2017.

1241 Jefferson, C. W., Thomas, D. J., Gandhi, S. S., Ramaekers, P., Delaney, G., Brisbin, D., Cutts, C., Portella, P., and
1242 Olson, R. A.: Unconformity-associated uranium deposits of the Athabasca Basin, Saskatchewan and Alberta,
1243 <https://doi.org/10.4095/223744>, 2007c.

1244 Jegal, Y., Zimmermann, C., Reisberg, L., Yeghicheyan, D., Cloquet, C., Peiffert, C., Gerardin, M., Deloule, E., and
1245 Mercadier, J.: Characterisation of Reference Materials for In Situ Rb-Sr Dating by LA-ICP-MS / MS, Geostandard
1246 Geoanalytic Res, 46, 645-671, <https://doi.org/10.1111/ggr.12456>, 2022.

1247 Jenkin, G. R. T., Ellam, R. M., Rogers, G., and Stuart, F. M.: An investigation of closure temperature of the biotite
1248 Rb-Sr system: The importance of cation exchange, Geochimica et Cosmochimica Acta, 65, 1141-1160,
1249 [https://doi.org/10.1016/S0016-7037\(00\)00560-3](https://doi.org/10.1016/S0016-7037(00)00560-3), 2001.



1250 Juhász, A., Tóth, T. M., Ramseyer, K., and Matter, A.: Connected fluid evolution in fractured crystalline basement
1251 and overlying sediments, Pannonian Basin, SE Hungary, Chemical Geology, 182, 91-120,
1252 [https://doi.org/10.1016/S0009-2541\(01\)00269-8](https://doi.org/10.1016/S0009-2541(01)00269-8), 2002.

1253 Kaczowka, A. J., Kyser, T. K., Kotzer, T. G., Leybourne, M. I., and Layton-Matthews, D.: Geometallurgical ore
1254 characterization of the high-grade polymetallic unconformity-related uranium deposit, The Canadian Mineralogist,
1255 59, 813-845, <https://doi.org/10.3749/canmin.2000050>, 2021.

1256 Kalt, A., Grauert, B., and Baumann, A.: Rb-Sr and U-Pb isotope studies on migmatites from the Schwarzwald
1257 (Germany): constraints on isotopic resetting during Variscan high-temperature metamorphism, Journal
1258 Metamorphic Geology, 12, 667-680, <https://doi.org/10.1111/j.1525-1314.1994.tb00050.x>, 1994.

1259 Karlstrom, K.: Refining Rodinia: Geologic Evidence for the Australia-Western U.S. connection in the Proterozoic,
1260 GSAT, 9, 1-7, <https://doi.org/10.1130/GSAT-1999-10-01-science>, 1999.

1261 Kister, P.: Mobilité des éléments géochimiques dans un bassin sédimentaire clastique, du Proterozoïque à nos
1262 jours : le bassin Athabasca (Saskatchewan, Canada), phdthesis, Institut National Polytechnique de Lorraine, 2003.

1263 Kister, P., Vieillard, P., Cuney, M., Quirt, D., and Laverret, E.: Thermodynamic constraints on the mineralogical
1264 and fluid composition evolution in a clastic sedimentary basin: the Athabasca Basin (Saskatchewan, Canada), ejm,
1265 17, 325-341, <https://doi.org/10.1127/0935-1221/2005/0017-0325>, 2005.

1266 Kohn, M.: Titanite Petrochronology, Reviews in Mineralogy and Geochemistry, 2017.

1267 Kotzer, T. G. and Kyser, T. K.: Fluid history of the Athabasca Basin and its relation to uranium deposits.
1268 Saskatchewan Energy and Mines, Saskatchewan Geological Survey Miscellaneous Report, 90, 153-157, 1990.

1269 Kotzer, T. G. and Kyser, T. K.: Petrogenesis of the Proterozoic Athabasca Basin, northern Saskatchewan, Canada,
1270 and its relation to diagenesis, hydrothermal uranium mineralization and paleohydrogeology, Chemical Geology,
1271 120, 45-89, [https://doi.org/10.1016/0009-2541\(94\)00114-N](https://doi.org/10.1016/0009-2541(94)00114-N), 1995.

1272 Kyser, K., Cuney, M.: Basins and uranium deposits, In: Geology and Geochemistry of Uranium and Thorium
1273 Deposits, Short Course Series, 46. pp. 224-250, 2015.

1274 Kyser, K., Lahusen, L., Drever, G., Dunn, C., Leduc, E., and Chipley, D.: Using Pb isotopes in surface media to
1275 distinguish anthropogenic sources from undercover uranium sources, Comptes Rendus. Géoscience, 347, 215-226,
1276 2015.

1277 Kyser, K., Hiatt, E., Renac, C., Durocher, K., Holk, G., and Deckart, K.: Diagenetic fluids in Paleo- and Meso-
1278 Proterozoic sedimentary basins and their implications for long protracted fluid histories.,
1279 <https://doi.org/10.13140/2.1.1033.1847>, 2005.

1280 Lacombe, O., Tavani, S., Lamarche, J., Balsamo, F., and Agosta, F.: Introduction: Faults and fractures in rocks:
1281 mechanics, occurrence, dating, stress history and fluid flow, Geol. Mag., 159, 1847-1854,
1282 <https://doi.org/10.1017/S0016756823000031>, 2022.

1283 Larsen, R. T. and Sundvoll: Rb-Sr isotope systematics In the magmatic rocks of the Oslo Rift, 2008.



1284 Laverret, E., Clauer, N., Fallick, A., Patrier Mas, P., Beaufort, D., Quirt, D., Kister, P., and Bruneton, P.: K-Ar
1285 dating and stable isotope tracing of illite associated with the Sea Creek unconformity-type uranium deposits
1286 (Athabasca Basin, Canada), in: "Bridging Clays" Joint meeting CMS/GFA, Oléron, France, 164, 2006.

1287 Liebmann, J., Kirkland, C. L., Kelsey, D. E., Korhonen, F. J., and Rankenburg, K.: Lithological fabric as a proxy
1288 for Rb-Sr isotopic complexity, Chemical Geology, 608, 121041, <https://doi.org/10.1016/j.chemgeo.2022.121041>,
1289 2022.

1290 Liu, W., Zhang, X., Zhang, J., and Jiang, M.: Sphalerite Rb-Sr Dating and in situ Sulfur Isotope Analysis of the
1291 Daliangzi Lead-Zinc Deposit in Sichuan Province, SW China, J. Earth Sci., 29, 573-586,
1292 <https://doi.org/10.1007/s12583-018-0785-5>, 2018.

1293 Macdonald, C. C.: Mineralogy and geochemistry of a precambrian regolith in the Athabasca Basin, 1980.

1294 Mao, G., Hua, R., Long, G., and Lu, H.: Rb-Sr Dating of Pyrite and Quartz Fluid Inclusions and Origin of Ore-
1295 forming Materials of the Jinshan Gold Deposit, Northeast Jiangxi Province, South China, Acta Geologica Sinica
1296 (Eng), 87, 1658-1667, <https://doi.org/10.1111/1755-6724.12166>, 2013.

1297 McLachlan, G. and Peel, D.: Finite Mixture Models, 1st ed., Wiley, <https://doi.org/10.1002/0471721182>, 2000.

1298 Martz, P.: Caractéristiques, chronologie et rôles des circulations fluides dans le bassin d'Athabasca et son socle :
1299 implications dans la formation et l'évolution du gisement d'uranium de Cigar Lake, These de doctorat, Université
1300 de Lorraine, 2017.

1301 Martz, P., Mercadier, J., Cathelineau, M., Boiron, M.-C., Quirt, D., Doney, A., Gerbeaud, O., De Wally, E., and
1302 Ledru, P.: Formation of U-rich mineralizing fluids through basinal brine migration within basement-hosted shear
1303 zones: A large-scale study of the fluid chemistry around the unconformity-related Cigar Lake U deposit
1304 (Saskatchewan, Canada), Chemical Geology, 508, 116-143, <https://doi.org/10.1016/j.chemgeo.2018.05.042>,
1305 2019a.

1306 Martz, P., Mercadier, J., Perret, J., Villeneuve, J., Deloule, E., Cathelineau, M., Quirt, D., Doney, A., and Ledru,
1307 P.: Post-crystallization alteration of natural uraninites: Implications for dating, tracing, and nuclear forensics,
1308 Geochimica et Cosmochimica Acta, 249, 138-159, <https://doi.org/10.1016/j.gca.2019.01.025>, 2019b.

1309 Matheney, R. K., Brookins, D. G., Wallin, E. T., Shafiqullah, M., and Damon, P. E.: Incompletely reset Rb • Sr
1310 systems from a Cambrian red-rock granophyre terrane, Florida Mountains, New Mexico, U.S.A., Chemical
1311 Geology: Isotope Geoscience section, 86, 29-47, [https://doi.org/10.1016/0168-9622\(90\)90004-V](https://doi.org/10.1016/0168-9622(90)90004-V), 1990.

1312 Melnykov, V. and Melnykov, I.: Initializing the EM algorithm in Gaussian mixture models with an unknown
1313 number of components, Computational Statistics & Data Analysis, 56, 1381-1395,
1314 <https://doi.org/10.1016/j.csda.2011.11.002>, 2012.

1315 Mcfarlane, C. and Markharrison, T.: Pb-diffusion in monazite: Constraints from a high-T contact aureole setting,
1316 Earth and Planetary Science Letters, 250, 376-384, <https://doi.org/10.1016/j.epsl.2006.06.050>, 2006.

1317 McGill BD, Marlat JL, Matthews RB, Sopuck VJ, Homeniuk LA, Hubregtse JJ.: The P2 North uranium deposit,
1318 Saskatchewan, Canada, Explor Min Geol., 2(4), 321-331, 1993



1319 McLachlan, G. J., Lee, S. X., and Rathnayake, S. I.: Finite Mixture Models, *Annual Review of Statistics and Its*
1320 *Application*, 6, 355-378, <https://doi.org/10.1146/annurev-statistics-031017-100325>, 2019.

1321 Menier, A., Roy, R., Harrison, G., Zerff, R. W., and Kinar, D.: Relationship between rock physical properties and
1322 spectral mineralogy applied to exploration for an unconformity-related uranium deposit (Saskatchewan, Canada),
1323 *Can. J. Earth Sci.*, 57, 1349-1364, <https://doi.org/10.1139/cjes-2019-0080>, 2020.

1324 Mercadier, J., Cuney, M., Cathelineau, M., and Lacorde, M.: U redox fronts and kaolinisation in basement-hosted
1325 unconformity-related U ores of the Athabasca Basin (Canada): late U remobilisation by meteoric fluids, *Miner*
1326 *Deposita*, 46, 105-135, <https://doi.org/10.1007/s00126-010-0314-7>, 2011.

1327 Mercadier, J., Richard, A., and Cathelineau, M.: Boron- and magnesium-rich marine brines at the origin of giant
1328 unconformity-related uranium deposits: $\delta^{11}\text{B}$ evidence from Mg-tourmalines, *Geology*, 40, 231-234,
1329 <https://doi.org/10.1130/G32509.1>, 2012.

1330 Mlynarska, M., Barnes, C. J., Zack, T., Majka, J., and Mazur, S.: In situ white mica Rb/Sr geochronology of the
1331 Leszczyniec metaigneous complex, West Sudetes: evidence of upper plate deformation at the onset of Variscan
1332 collision, *Int J Earth Sci (Geol Rundsch)*, 113, 319-333, <https://doi.org/10.1007/s00531-023-02373-8>, 2024.

1333 Muñoz-Montecinos, J., Giuliani, A., Oesch, S., Volante, S., Peters, B., and Behr, W.: In situ rubidium-strontium
1334 geochronology of white mica in young metamorphic and metasomatic rocks from Syros: testing the limits of laser-
1335 ablation triple-quadrupole inductively coupled plasma mass spectrometer mica dating using different anchoring
1336 approaches, *Geochronology*, 6, 585-605, <https://doi.org/10.5194/gchron-6-585-2024>, 2024.

1337 Ng, R., Alexandre, P., Kyser, K., Cloutier, J., Abdu, Y. A., and Hawthorne, F. C.: Oxidation state of iron in alteration
1338 minerals associated with sandstone-hosted unconformity-related uranium deposits and apparently barren alteration
1339 systems in the Athabasca Basin, Canada: Implications for exploration, *Journal of Geochemical Exploration*, 130,
1340 22-43, <https://doi.org/10.1016/j.gexplo.2013.02.009>, 2013.

1341 Nguyen, H. and McLachlan, G.: Maximum likelihood estimation of Gaussian mixture models without matrix
1342 operations, *Advances in Data Analysis and Classification*, 9, <https://doi.org/10.1007/s11634-015-0209-7>, 2015.

1343 Obin, T.: Mobilités du carbone et du soufre dans l'environnement du Bassin de l'Athabasca (Saskatchewan,
1344 Canada) et impact(s) sur la formation des gisements d'uranium de type discordance, *These de doctorat*, Université
1345 de Lorraine, 2025.

1346 Olierook, H. K. H., Rankenburg, K., Ulrich, S., Kirkland, C. L., Evans, N. J., Brown, S., McInnes, B. I. A., Prent,
1347 A., Gillespie, J., McDonald, B., and Darragh, M.: Resolving multiple geological events using in situ Rb-Sr
1348 geochronology: implications for metallogenesis at Tropicana, Western Australia, *Geochronology*, 2, 283-303,
1349 <https://doi.org/10.5194/gchron-2-283-2020>, 2020.

1350 Oummouch, A., Essaifi, A., Zayane, R., Maddi, O., Zouhair, M., and Maacha, L.: Geology and Metallogenesis of
1351 the Sediment-Hosted Cu-Ag Deposit of Tizert (Igherm Inlier, Anti-Atlas Copperbelt, Morocco), *Geofluids*, 2017,
1352 7508484, <https://doi.org/10.1155/2017/7508484>, 2017.



1353 Pacquet, A. and Weber, F.: Pétrographie et minéralogie des halos d'altération autour du gisement de Cigar Lake et
1354 leurs relations avec les minéralisations, *Can. J. Earth Sci.*, 30, 674-688, <https://doi.org/10.1139/e93-055>, 1993.

1355 Paton, C., Hellstrom, J., Paul, B., Woodhead, J., and Hergt, J.: Iolite: Freeware for the visualisation and processing
1356 of mass spectrometric data, *J. Anal. At. Spectrom.*, 26, 2508-2518, <https://doi.org/10.1039/C1JA10172B>, 2011.

1357 Pehrsson, S., Eglington, B., Rainbird, R., Regis, D., Ramaekers, P., and Jefferson, C.: Extent and significance of
1358 the Racklan-Forward Orogen in Canada: far-field interior reactivation during Nuna assembly, *SP*, 531, 47-75,
1359 <https://doi.org/10.1144/SP531-2022-307>, 2023.

1360 Percival, J. B. and Kodama, H.: Sudoite from cigar lake, Saskatchewan, *The Canadian Mineralogist*, 27, 633-641,
1361 1989.

1362 Philippe, S., Lancelot, J. R., Clauer, N., and Pacquet, A.: Formation and evolution of the Cigar Lake uranium
1363 deposit based on U-Pb and K-Ar isotope systematics, *Can. J. Earth Sci.*, 30, 720-730, <https://doi.org/10.1139/e93-058>, 1993.

1365 Powell, J. W., Percival, J. B., Potter, E. G., Van Der Lelij, R., and Xie, R.: Mineralogy and K-Ar geochronology
1366 of clay alteration associated with uranium mineralization in the Patterson Lake Corridor, Saskatchewan, *GEEA*,
1367 22, [geochem2021-061](https://doi.org/10.1144/geochem2021-061), <https://doi.org/10.1144/geochem2021-061>, 2022.

1368 Rabiei, M., Chi, G., Normand, C., Davis, W. J., Fayek, M., and Blamey, N. J. F.: Hydrothermal Rare Earth Element
1369 (Xenotime) Mineralization at Maw Zone, Athabasca Basin, Canada, and Its Relationship to Unconformity-Related
1370 Uranium Deposits, *Economic Geology*, 112, 1483-1507, <https://doi.org/10.5382/econgeo.2017.4518>, 2017.

1371 Rainbird, R. H., Stern, R. A., Rayner, N., Jefferson, C. W., and Delaney, G.: Age, provenance, and regional
1372 correlation of the Athabasca Group, Saskatchewan and Alberta, constrained by igneous and detrital zircon
1373 geochronology, *Bulletin-Geological Survey of Canada*, 588, 193, 2007.

1374 Ramaekers, P., Jefferson, C. W., Yeo, G. M., Collier, B., Long, D. G. F., Drever, G., McHardy, S., Jiricka, D., Cutts,
1375 C., and Wheatley, K.: Revised geological map and stratigraphy of the Athabasca Group, Saskatchewan and Alberta,
1376 *Bulletin-Geological Survey of Canada*, 588, 155, 2007.

1377 Rasmussen, B., Fletcher, I. R., and McNaughton, N. J.: Dating low-grade metamorphic events by SHRIMP U-Pb
1378 analysis of monazite in shales, *Geol.*, 29, 963, [https://doi.org/10.1130/0091-7613\(2001\)029%253C0963:DLGMEB%253E2.0.CO;2](https://doi.org/10.1130/0091-7613(2001)029%253C0963:DLGMEB%253E2.0.CO;2), 2001.

1380 Rasmussen, B., Sheppard, S., and Fletcher, I. R.: Testing ore deposit models using in situ U-Pb geochronology of
1381 hydrothermal monazite: Paleoproterozoic gold mineralization in northern Australia, *Geology*, 34, 77-80,
1382 <https://doi.org/10.1130/G22058.1>, 2006.

1383 Rasmussen, B., Zi, J.-W., and Muhling, J. R.: Tectonic fluid expulsion: U-Pb evidence for punctuated hydrothermal
1384 fluid flow and hydraulic fracturing during orogenesis, *Earth and Planetary Science Letters*, 604, 117997,
1385 <https://doi.org/10.1016/j.epsl.2023.117997>, 2023.

1386 Redaa, A., Farkaš, J., Gilbert, S., Collins, A. S., Wade, B., Löhr, S., Zack, T., and Garbe-Schönberg, D.: Assessment
1387 of elemental fractionation and matrix effects during in situ Rb-Sr dating of phlogopite by LA-ICP-MS/MS:



1388 implications for the accuracy and precision of mineral ages, *J. Anal. At. Spectrom.*, 36, 322-344,
1389 <https://doi.org/10.1039/D0JA00299B>, 2021.

1390 Redaa, A., Farkaš, J., Hassan, A., Collins, A. S., Gilbert, S., and Löhr, S. C.: Constraints from in-situ Rb-Sr dating
1391 on the timing of tectono-thermal events in the Umm Farwah shear zone and associated Cu-Au mineralisation in
1392 the Southern Arabian Shield, Saudi Arabia, *Journal of Asian Earth Sciences*, 224, 105037,
1393 <https://doi.org/10.1016/j.jseas.2021.105037>, 2022.

1394 Reynolds, R. C. and Thomson, C. H.: Illite from the Potsdam Sandstone of New York: A Probable
1395 Noncentrosymmetric Mica Structure, *Clays and clay miner.*, 41, 66-72,
1396 <https://doi.org/10.1346/CCMN.1993.0410107>, 1993.

1397 Ribeiro, B. V., Kirkland, C. L., Finch, M. A., Faleiros, F. M., Reddy, S. M., Rickard, W. D. A., and Hartnady, M.
1398 I. H.: Microstructures, geochemistry, and geochronology of mica fish: Review and advances, *Journal of Structural
1399 Geology*, 175, 104947, <https://doi.org/10.1016/j.jsg.2023.104947>, 2023a.

1400 Ribeiro, B. V., Kirkland, C. L., Kelsey, D. E., Reddy, S. M., Hartnady, M. I. H., Faleiros, F. M., Rankenburg, K.,
1401 Liebmann, J., Korhonen, F. J., and Clark, C.: Time-strain evolution of shear zones from petrographically
1402 constrained Rb-Sr muscovite analysis, *Earth and Planetary Science Letters*, 602, 117969,
1403 <https://doi.org/10.1016/j.epsl.2022.117969>, 2023b.

1404 Richard, A., Banks, D. A., Mercadier, J., Boiron, M.-C., Cuney, M., and Cathelineau, M.: An evaporated seawater
1405 origin for the ore-forming brines in unconformity-related uranium deposits (Athabasca Basin, Canada): Cl/Br and
1406 ^{83}Cl analysis of fluid inclusions, *Geochimica et Cosmochimica Acta*, 75, 2792-2810,
1407 <https://doi.org/10.1016/j.gca.2011.02.026>, 2011.

1408 Richard, A., Cauzid, J., Cathelineau, M., Boiron, M. -C., Mercadier, J., and Cuney, M.: Synchrotron XRF and
1409 XANES investigation of uranium speciation and element distribution in fluid inclusions from unconformity-related
1410 uranium deposits, *Geofluids*, 13, 101-111, <https://doi.org/10.1111/gfl.12009>, 2013.

1411 Richard, A., Montel, J.-M., Leborgne, R., Peiffert, C., Cuney, M., and Cathelineau, M.: Monazite Alteration in
1412 $H_2O \pm HCl \pm NaCl \pm CaCl_2$ Fluids at 150 °C and psat: Implications for Uranium Deposits, *Minerals*, 5, 693-706,
1413 <https://doi.org/10.3390/min5040518>, 2015.

1414 Rösel, D. and Zack, T.: LA-ICP-MS/MS Single-Spot Rb-Sr Dating, *Geostandard Geoanalytic Res*, 46, 143-168,
1415 <https://doi.org/10.1111/ggr.12414>, 2022.

1416 Saito, T., Qiu, H.-N., Shibuya, T., Li, Y.-B., Kitajima, K., Yamamoto, S., Ueda, H., Komiya, T., and Maruyama,
1417 S.: Ar-Ar dating for hydrothermal quartz from the 2.4 Ga Ongeluk Formation, South Africa: implications for
1418 seafloor hydrothermal circulation, *R Soc Open Sci*, 5, 180260, <https://doi.org/10.1098/rsos.180260>, 2018.

1419 Schneider, D. A., Heizler, M. T., Bickford, M. E., Wortman, G. L., Condie, K. C., and Perilli, S.: Timing constraints
1420 of orogeny to cratonization: Thermochronology of the Paleoproterozoic Trans-Hudson orogen, Manitoba and
1421 Saskatchewan, Canada, *Precambrian Research*, 153, 65-95, <https://doi.org/10.1016/j.precamres.2006.11.007>,
1422 2007.



1423 Scott Anderson, F., Levine, J., and Whitaker, T. J.: Rb-Sr resonance ionization geochronology of the Duluth
1424 Gabbro: A proof of concept for in situ dating on the Moon, *Rapid Communications in Mass Spectrometry*, 29,
1425 1457-1464, <https://doi.org/10.1002/rclm.7253>, 2015.

1426 Sengün, F., Bertrandsson Erlandsson, V., Hogmalm, J., and Zack, T.: In situ Rb-Sr dating of K-bearing minerals
1427 from the orogenic Akçaabat gold deposit in the Menderes Massif, Western Anatolia, Turkey, *Journal of Asian Earth*
1428 *Sciences*, 185, 104048, <https://doi.org/10.1016/j.jseaes.2019.104048>, 2019.

1429 Schmitz, B., Biermanns, P., Hueck, M., Wemmer, K., Schmid, S. M., Onuzi, K., Reicherter, K., and Ustaszewski,
1430 K.: Kinematics and Age of the Orogen-Perpendicular Shkoder-Peja Normal Fault in North Albania Constrained
1431 by Fault-Slip Data, Raman Spectroscopy and K-Ar Fault-Gouge Dating, *Tectonics*, 44, e2024TC008660,
1432 <https://doi.org/10.1029/2024TC008660>, 2025.

1433 Skirrow, R. G., Mercadier, J., Armstrong, R., Kuske, T., and Deloule, E.: The Ranger uranium deposit, northern
1434 Australia: Timing constraints, regional and ore-related alteration, and genetic implications for unconformity-
1435 related mineralisation, *Ore Geology Reviews*, 76, 463-503, <https://doi.org/10.1016/j.oregeorev.2015.09.001>, 2016.

1436 Sibson, R. H.: Conditions for fault-valve behaviour, *SP*, 54, 15-28,
1437 <https://doi.org/10.1144/GSL.SP.1990.054.01.02>, 1990.

1438 Sims, P. K. and Petermar, Z. E.: Early Proterozoic Central Plains orogen: A major buried structure in the north-
1439 central United States, *Geology*, 14, 488-491, [https://doi.org/10.1130/0091-7613\(1986\)14%253C488:EPCPOA%253E2.0.CO;2](https://doi.org/10.1130/0091-7613(1986)14%253C488:EPCPOA%253E2.0.CO;2), 1986.

1441 Skipton, D. R., St-Onge, M. R., Schneider, D. A., and McFarlane, C. R. M.: Tectonothermal Evolution of the
1442 Middle Crust in the Trans-Hudson Orogen, Baffin Island, Canada: Evidence from Petrology and Monazite
1443 Geochronology of Sillimanite-bearing Migmatites, *Journal of Petrology*, 57, 1437-1462,
1444 <https://doi.org/10.1093/petrology/egw046>, 2016.

1445 Tian, J., Wang, J., Tian, T., Wang, L., Wang, Y., Yu, X., Zhang, W., Ren, T., and Sun, B.: In-Situ Geochemical and
1446 Rb-Sr Dating Analysis of Sulfides from a Gold Deposit Offshore of Northern Sanshandao, Jiaodong Peninsula,
1447 North China: Implications for Gold Mineralization, *Minerals*, 14, 456, <https://doi.org/10.3390/min14050456>,
1448 2024.

1449 Tichomirowa, M., Käßner, A., Sperner, B., Lapp, M., Leonhardt, D., Linnemann, U., Münker, C., Ovtcharova, M.,
1450 Pfänder, J. A., Schaltegger, U., Sergeev, S., von Quadt, A., and Whitehouse, M.: Dating multiply overprinted
1451 granites: The effect of protracted magmatism and fluid flow on dating systems (zircon U-Pb: SHRIMP/SIMS, LA-
1452 ICP-MS, CA-ID-TIMS; and Rb-Sr, Ar-Ar) - Granites from the Western Erzgebirge (Bohemian Massif, Germany),
1453 *Chemical Geology*, 519, 11-38, <https://doi.org/10.1016/j.chemgeo.2019.04.024>, 2019.

1454 Tran, H., Ansdell, K., Bethune, K., Ashton, K., and Hamilton, M.: Provenance and tectonic setting of
1455 Paleoproterozoic metasedimentary rocks along the eastern margin of Hearne craton: Constraints from SHRIMP
1456 geochronology, Wollaston Group, Saskatchewan, Canada, *Precambrian Research*, 167, 171-185,
1457 <https://doi.org/10.1016/j.precamres.2008.08.003>, 2008.



1458 Toma, J., Creaser, R. A., Card, C., Stern, R. A., Chacko, T., and Steele-MacInnis, M.: Re-Os systematics and
1459 chronology of graphite, *Geochimica et Cosmochimica Acta*, 323, 164-182,
1460 <https://doi.org/10.1016/j.gca.2022.02.012>, 2022.

1461 Toma, J., Creaser, R. A., Card, C., Pana, D., Dufrane, A., and Li, L.: Nuna supercontinent assembly linked to
1462 carbon cycling in shear zones 1.9-1.7 billion years ago, *Nat. Geosci.*, 17, 1038-1045,
1463 <https://doi.org/10.1038/s41561-024-01519-w>, 2024.

1464 Velde, B. and Christophe, R.: Smectite to illite conversion and K-AR ages, *Clay Minerals*, 31, 25-32, 1996.

1465 Vermeesch, P.: IsoplotR: A free and open toolbox for geochronology, *Geoscience Frontiers*, 9, 1479-1493,
1466 <https://doi.org/10.1016/j.gsf.2018.04.001>, 2018.

1467 Villa: Isotopic closure, *Terra Nova*, 10, 42-47, <https://doi.org/10.1046/j.1365-3121.1998.00156.x>, 1998.

1468 Viswanathan, H. S., Ajo-Franklin, J., Birkholzer, J. T., Carey, J. W., Guglielmi, Y., Hyman, J. D., Karra, S., Pyrak-
1469 Nolte, L. J., Rajaram, H., Srinivasan, G., and Tartakovsky, D. M.: From Fluid Flow to Coupled Processes in
1470 Fractured Rock: Recent Advances and New Frontiers, *Reviews of Geophysics*, 60, e2021RG000744,
1471 <https://doi.org/10.1029/2021RG000744>, 2022.

1472 Walter, B., Géraud, Y., Bartier, D., Kluska, J.-M., Diraison, M., Morlot, C., and Raisson, F.: Petrophysical and
1473 mineralogical evolution of weathered crystalline basement in western Uganda: Implications for fluid transfer and
1474 storage, *Bulletin*, 102, 1035-1065, <https://doi.org/10.1306/0810171610917171>, 2018.

1475 Wang, C., Alard, O., Lai, Y.-J., Foley, S. F., Liu, Y., Munnikhuis, J., and Wang, Y.: Advances in in-situ Rb-Sr dating
1476 using LA-ICP-MS/MS: applications to igneous rocks of all ages and to the identification of unrecognized
1477 metamorphic events, *Chemical Geology*, 610, 121073, <https://doi.org/10.1016/j.chemgeo.2022.121073>, 2022.

1478 Weinberg, R. F., Wolfram, L. C., Nebel, O., Hasalová, P., Závada, P., Kylander-Clark, A. R. C., and Becchio, R.:
1479 Decoupled U-Pb date and chemical zonation of monazite in migmatites: The case for disturbance of isotopic
1480 systematics by coupled dissolution-reprecipitation, *Geochimica et Cosmochimica Acta*, 269, 398-412,
1481 <https://doi.org/10.1016/j.gca.2019.10.024>, 2020.

1482 Willigers, B. J. A., Mezger, K., and Baker, J. A.: Development of high precision Rb-Sr phlogopite and biotite
1483 geochronology; an alternative to 40Ar/39Ar tri-octahedral mica dating, *Chemical Geology*, 213, 339-358,
1484 <https://doi.org/10.1016/j.chemgeo.2004.07.006>, 2004.

1485 Woodhead, J. D. and Hergt, J. M.: Strontium, Neodymium and Lead Isotope Analyses of NIST Glass Certified
1486 Reference Materials: SRM 610, 612, 614, *Geostandards Newsletter*, 25, 261-266, <https://doi.org/10.1111/j.1751-908X.2001.tb00601.x>, 2001.

1488 Worden, J.M., Cumming, G.L., and Baadsgaard, H.: Geochronology of host rocks and mineralization of the
1489 Midwest uranium deposit, northern Saskatchewan, In: Sibbald, T.I., Petruk, W. (Eds.), *Geology of Uranium*
1490 Deposits, Canadian Institute of Mining and Metallurgy, 32, 67-72, 1985.

1491 Yardley, B. W. D.: Quartz veins and devolatilization during metamorphism, *JGS*, 140, 657-663,
1492 <https://doi.org/10.1144/gsjgs.140.4.0657>, 1983.



1493 Yardley, B. W. D. and Bodnar, R. J.: Fluids in the Continental Crust, *GeochemPersp*, 3, 1-127,
1494 <https://doi.org/10.7185/geochempersp.3.1>, 2014.

1495 Yeo, G. M. and Delaney, G.: The Wollaston Supergroup, stratigraphy and metallogeny of a Paleoproterozoic
1496 Wilson cycle in the Trans-Hudson Orogen, Saskatchewan, <https://doi.org/10.4095/223746>, 2007.

1497 Zack, T. and Hogmalm, K. J.: Laser ablation Rb/Sr dating by online chemical separation of Rb and Sr in an oxygen-
1498 filled reaction cell, *Chemical Geology*, 437, 120-133, <https://doi.org/10.1016/j.chemgeo.2016.05.027>, 2016.

1499 Zametzer, A., Kirkland, C. L., Barham, M., Hartnady, M. I. H., Bath, A. B., and Rankenburg, K.: Episodic alteration
1500 within a gold-bearing Archean shear zone revealed by in situ biotite Rb-Sr dating, *Precambrian Research*, 382,
1501 106872, <https://doi.org/10.1016/j.precamres.2022.106872>, 2022.

1502